A periplasmic protein complex mediates cell envelope integrity and intrinsic multidrug resistance in *Mycobacterium tuberculosis*

Thaís Klevorn[1,2], Christopher Brown[3*], Christine D. Hardy[4*], Bonnie J. Cuthbert[4*], Amanda Spencer[5], Adrián Jinich[5], Luming Chan[1], Jessica Mendoza[4], Rodger de Miranda[4], Heather Kim[1], Dirk Schnappinger[1], Kyu Rhee[2,3], Celia Goulding[4,6], Sabine Ehrt[1,2+]

[1]Department of Microbiology and Immunology, Weill Cornell Medical College, New York, NY, USA

[2]Immunology and Microbial Pathogenesis Graduate Program, Weill Cornell Graduate School of Medical Sciences, Cornell University, New York, New York, USA

[3]Department of Medicine, Weill Cornell Medical College, New York, New York, USA

[4]Department of Molecular Biology & Biochemistry, University of California Irvine, Irvine, California, USA

[5]Department of Chemistry & Biochemistry, Skaggs School of Pharmacy & Pharmaceutical Sciences, University of California San Diego, San Diego, California, USA

[6]Department of Pharmaceutical Sciences, University of California Irvine, Irvine, California, USA

*These authors contributed equally.

[+]Corresponding author.

Abstract

The intrinsic drug resistance of *Mycobacterium tuberculosis* (Mtb) is a major barrier to effective tuberculosis (TB) treatment and is largely attributed to its complex, impermeable cell envelope. We identified a periplasmic protein complex comprising FecB and Rv3035 that is essential for maintaining cell envelope integrity and mediating intrinsic multidrug resistance in Mtb. FecB interacts directly with Rv3035, forming a stable heterodimer that also associates with the cell envelope biosynthesis proteins AftB and Rv0227c. We report the structures of Rv3035 alone and in complex with FecB, and identify critical residues required for complex formation and function. Co-essentiality analysis and genetic interaction experiments further supported a functional link between FecB, Rv3035 and AftB, the enzyme responsible for the last step in the biosynthesis of the cell envelope components arabinogalactan and lipoarabinomannan. Mtb mutants of *fecB*, *rv3035* and *aftB* accumulated trehalose monomycolates in the outer membrane, consistent with a perturbation of membrane assembly and/or maintenance. Importantly, we show that FecB is required for Mtb virulence in mice, underscoring its physiological relevance. Altogether, our findings uncover a previously uncharacterized periplasmic protein complex that supports cell envelope integrity and intrinsic drug resistance in Mtb, highlighting FecB and Rv3035 as promising targets for therapeutic intervention.

Introduction

Tuberculosis (TB) remains the world's leading cause of death from a single infectious agent and is responsible for over 1 million deaths anually[1]. Unlike most bacterial infections, successful TB treatment requires multiple antibiotics taken for several months, even in drug-susceptible cases. This prolonged therapy is in part due to the intrinsic drug resistance of *Mycobacterium tuberculosis* (Mtb), the causative agent of TB[2]. A key contributor to this resistance is Mtb's complex, multi-layered cell envelope, which acts as a protective barrier against antibiotics and host immune defenses[3]. Despite its central role in Mtb's pathogenicity and drug resistance, the molecular mechanisms governing the structure, assembly, and function of the mycobacterial cell envelope remain incompletely understood[4].

To identify novel targets that could potentiate existing TB therapies and shorten treatment duration, we previously performed a genome-wide chemical-genetic screen using transposon mutagenesis and sequencing[5]. This identified *fecB* (Rv3044) as a gene whose disruption sensitized Mtb to multiple antibiotics that have various mechanisms of action. These included rifampicin and ethambutol, which are part of the standard treatment regimen for drug susceptible TB, and pretomanid which is part of the BPaL (bedaquiline, pretomanid, linezolid) regimen used to treat drug-resistant TB[5]. Functional studies of a Mtb *fecB* knockout strain (Δ*fecB*) revealed that *fecB* is essential for maintaining the impermeability of the Mtb cell envelope [5].

In Mtb, FecB is annotated as a periplasmic substrate-binding protein homologous to FecB from *Escherichia coli*, which mediates ferric citrate transport[6]. However, Mtb lacks several canonical components of the ferric citrate transport system. Instead, Mtb FecB binds heme and the siderophore carboxymycobactin and interacts with components of the mycobacterial siderophore transport machinery[7]. Despite these biochemical insights, the physiological role of FecB in Mtb is not fully defined. Here, we investigated how FecB contributes to Mtb's intrinsic antibiotic resistance and uncovered a critical functional interaction with Rv3035, a previously uncharacterized periplasmic protein. Rv3035 not only interacts with FecB, but also with AftB (Rv3805c), likely bridging these two proteins to form a larger complex that is important for cell envelope biogenesis.

Given the urgent need for shorter and more effective TB treatments, elucidating mechanisms that underlie Mtb's intrinsic drug resistance is of high therapeutic relevance[2,3]. By characterizing the function of FecB and Rv3035 in Mtb, this study advances our understanding of periplasmic proteins in mycobacteria and highlights these proteins as promising targets for combination therapies aimed at enhancing the efficacy of existing anti-TB drugs.

Results

Mtb∆*fecB* displays a transcriptional iron deprivation signature and accumulates siderophores

Transcriptome analysis can provide functional insights by identifying pathways that are differentially regulated in a mutant strain compared to a wild type (WT) strain. These changes

may reflect the mutant strain's need to adapt in the absence of the gene of interest[8]. To gain insight into the function of FecB, we performed transcriptomic analysis by RNA sequencing of Mtb WT, Δ*fecB* and a complemented strain (Δ*fecB::fecB,* containing a chromosomally integrated plasmid expressing *fecB* from the *hsp60* promoter). We decided to compare the transcriptional profile of the strains in regular growth conditions with detergent (0.05% Tween80) and without detergent, because the presence of Tween80, although helpful to prevent excessive clumping of mycobacterial cultures, also strips the mycobacterial capsule and some surface exposed lipids[9], making it a less physiologically relevant condition.

Compared to WT and the complemented strain, Δ*fecB* significantly upregulated the *iniBAC* operon, which is known to be induced in response to cell wall stress[10], both in the presence and absence of detergent in the medium (Fig. 1A and data S1). Furthermore, in detergent-free conditions, 61% of the upregulated (22 of 36) and 13% of downregulated (3 of 23) differentially expressed genes (DEGs) were related to iron utilization. The upregulated DEGs included all 14 siderophore biosynthesis genes (*mbtA-mbtN*), the genes that encode the IrtA/B transporter for siderophore uptake (*irtA*, *irtB*) and the ESX-3 secretion system substrates (*esxG*, *esxH*), which are required for mycobactin-mediated iron acquisition. The downregulated DEGs included *bfrB*, encoding the iron storage protein bacterioferritin (Fig. 1, A and B). When grown in detergent-free media, Δ*fecB* thus displays a transcriptional iron deprivation signature even though the media contains a high concentration of iron. This iron deprivation signature is conditional, and it was not present when Tween80 was included in the medium (Fig. 1A). One potential explanation for this difference in transcriptional response is that Tween80's stripping of the capsule and some outer membrane lipids might facilitate uptake of iron in Δ*fecB* during growth in regular media.

Further supporting the transcriptomics data, the iron starvation signature in Δ*fecB* in detergent-free medium was accompanied by an accumulation of cell-associated siderophores as identified by mass-spectrometry analysis of lipid extracts (Fig. 1C). Taken together, these data suggest that Δ*fecB* may be less efficient in acquiring iron in detergent-free media due to interrupted siderophore export through the periplasm, mycobacterial outer membrane and/or capsule.

FecB is non-critical for mycobactin-mediated iron acquisition in Mtb

To further probe FecB's potential role in iron acquisition, we analyzed the growth of Δ*fecB*, WT and Δ*fecB*::*fecB* in iron-limiting conditions (Fig. 1D). We included a siderophore mutant, MtbΔ*mbtK*, to ensure that the growth medium was iron limiting. After starving the strains for iron to deplete internal iron stores and then growing them in either high or low iron conditions (iron-chelated medium with 160 μM or 1 μM ammonium ferric citrate, respectively), we observed only a minor growth defect of Δ*fecB* compared to the control strains, both in the presence (Fig. 1D) or absence of detergent (fig. S1A). Upon passaging the strains growing in low iron into both high and low iron conditions, the growth defect was still subtle and much weaker than the strong growth defect of Δ*mbtK* (Fig. 1D).

FecB can bind to ferric- and apo-carboxymycobactin with high affinity *in vitro*, and this binding is disrupted by mutating key residues E339, R240 and Y242[7]. To test whether binding to siderophores is required for complementing Δ*fecB*'s iron-related phenotypes, we cloned and

117 expressed FecB variants harboring the mutations E339S together with R240S or Y242S in Δ*fecB*.
118 The FecB variants with significantly reduced binding affinity to ferric-carboxymycobactin
119 (E339S_R240S and E339S_Y242S) fully reversed the iron deprivation transcriptional signature
120 (examined by representative gene expression of *mbtB*, *ppe37* and *irtA*) in detergent-free media
121 (Fig. 1E), and the subtle growth defect in low iron (fig. S1B). This complementation was
122 particularly remarkable given that the variant proteins were not clearly detectable in whole cell
123 lysates via western blot (fig. S1C). However, we note that the FecB E339S_R240S and
124 E339S_Y242S double mutants bind apo-carboxymycobactin with similar (or slightly higher)
125 affinity than WT FecB (fig. S1D). Thus, we cannot rule out that binding apo-siderophores is an
126 important function of FecB.

127 Taken together, these results suggest that FecB plays a role in iron acquisition in Mtb, however,
128 the subtle growth defect of Δ*fecB* in iron-limiting conditions points to a condition-dependent non-
129 critical function that is likely compensated for by other gene products required for iron acquisition.

130

131 **FecB's role in intrinsic multidrug resistance is distinct from its activity in iron homeostasis**

132 FecB is critical for Mtb's cell envelope impermeability and resistance to multiple antibiotics[5]. To
133 test whether FecB's activity in iron homeostasis is related to its activity in mediating cell envelope
134 integrity and multidrug resistance in Mtb, we tested whether the FecB variants with reduced
135 binding to ferric-carboxymycobactin could rescue the antibiotic hypersusceptibility of Δ*fecB*.
136 Vancomycin and rifampicin were chosen for minimal inhibitory concentration (MIC) assays
137 because Δ*fecB* is significantly more susceptible to these drugs compared to WT[5].
138 Complementation of Δ*fecB* with the FecB double mutants (E339S_R240S and E339S_Y242S)
139 fully rescued Δ*fecB*'s hypersusceptibility to vancomycin and rifampicin (Fig. 2A) indicating that
140 ferric-carboxymycobactin binding is not required for FecB's function in mediating antibiotic
141 resistance.

142 To explore whether siderophore accumulation in Δ*fecB* (Fig. 1C) leads to antibiotic
143 hypersusceptibility, we interrupted siderophore biosynthesis via CRISPR interference (CRISPRi)
144 knock down (KD) of the mycobactin biosynthesis gene *mbtI* in Δ*fecB*. If siderophore accumulation
145 is directly related to increased antibiotic susceptibility in Δ*fecB*, reducing siderophore production
146 by knocking down *mbtI* should relieve this phenotype. We validated the KD of *mbtI* in WT and
147 Δ*fecB* backgrounds by growing the strains in iron-limiting conditions, in the presence or absence
148 of anhydrotetracycline (ATc) to activate CRISPRi (fig. S2A). In the presence of ATc, the *mbtI* KD
149 strains failed to grow with ammonium ferric citrate concentrations lower than 1 μM, similarly to
150 Δ*mbtK*, indicating that siderophore production is significantly impaired through silencing of *mbtI*.
151 We next measured the MICs of vancomycin and rifampicin against the *mbtI* KD strain, in the
152 presence or absence of ATc (Fig. 2B). Silencing *mbtI* with ATc did not alter the MICs, indicating
153 that siderophore accumulation is likely not the cause of antibiotic hypersusceptibility in Δ*fecB*.

154 To further test whether siderophores are involved in the antibiotic hypersusceptibility of Δ*fecB*, we
155 tested whether induction of siderophore biosynthesis would enhance Δ*fecB*'s susceptibility to
156 vancomycin and rifampicin. We performed MIC assays in low iron medium, where siderophore
157 synthesis is induced, and in regular medium, where siderophore synthesis is suppressed (Fig. 2C

158 and fig. S2B). Additionally, since an iron-starvation transcriptional signature, which includes the
159 overexpression of siderophore biosynthesis genes, was observed in Δ*fecB* only in the absence of
160 detergent (Fig. 1A), we also tested whether the mutant's antibiotic hypersusceptibility would
161 increase in detergent-free medium compared to medium containing 0.05% Tween80 (fig. S2C).
162 Contrary to these hypotheses, the differences of the vancomycin and rifampicin MICs against
163 Δ*fecB* compared to WT and Δ*fecB*::*fecB* decreased in low iron medium compared to regular iron
164 rich medium (Fig. 2C). Similarly, a reduced shift in MICs was observed in detergent-free conditions
165 (fig. S2C). These results do not support a direct involvement of siderophores in the antibiotic
166 hypersusceptibility phenotype of Δ*fecB.* The reduced differences in antibiotic MICs might be due
167 to slowed growth rates of the strains in low iron medium and increased clumping in detergent-free
168 medium, which hinder accurate optical density measurements. In summary, these experiments
169 dissociate FecB's role in iron homeostasis from that in antibiotic resistance.

170

171 **FecB and Rv3035 interact in Mtb and likely function in the same cellular pathway**

172 FecB is classified as a periplasmic substrate-binding protein that has been shown to interact with
173 siderophore-mediated iron transport proteins[7]. Since our data point to an alternative role for FecB
174 in mediating intrinsic drug resistance in Mtb, we set out to identify additional physical interactors
175 of FecB that could shed light on other pathways in which FecB might participate. Pull-down and
176 mass spectrometry analysis of FLAG-tagged FecB was performed and analyzed compared to the
177 pull-down of an WT lysate control to eliminate non-specific interactions.

178 The most highly enriched interactor in our dataset was the uncharacterized protein Rv3035 (Fig.
179 3A). Rv3035 is annotated as an essential hypothetical protein containing WD40 repeats that
180 together are predicted to form an eight-bladed β-propeller structure. These domains can serve as
181 scaffolds in protein-protein interactions and the formation of multiprotein complexes and play
182 important roles in prokaryotes and eukaryotes[11]. We confirmed binding of FecB to Rv3035 by co-
183 immunoprecipitation of the tagged proteins (fig. S3) and then set out to identify Rv3035's physical
184 interactors by using Rv3035 as the bait in a second pull-down experiment. Satisfyingly, FecB was
185 the most enriched protein in the pull-down of Rv3035-3xFLAG, compared to the WT lysate control
186 (Fig. 3B). In addition, AftB and Rv0227c, which are the other two most enriched interacting
187 partners of FecB, were also among the most enriched partners of Rv3035 (Fig. 3, A and B, and
188 data S2).

189 To further inform our proteomics findings, we investigated the genetic interactions of *fecB* via co-
190 essentiality/co-fitness analysis. This method allows the detection of gene pairs that share similar
191 fitness profiles across forward genetic screens, and thus, can help identify genes that encode
192 proteins with similar or related function[12]. Using a publicly available CRISPRi chemical-genetic
193 interaction dataset which profiled gene essentiality across 80 drug-treatment and CRISPRi pre-
194 depletion conditions[13], we performed co-essentiality analysis using generalized least squares
195 (GLS) regression of *fecB*, *rv3035*, and the genes encoding their most enriched common protein
196 interactors, *aftB* and *rv0227c*. While *rv0227c* did not share an essentiality profile with the others,
197 *fecB*, *rv3035* and *aftB* were all hits in each other's co-essential gene clusters (Fig. 3, C and D).

198 This analysis identified 13 genes co-essential with *fecB*, 19 with *rv3035* and 22 with *aftB*, among
199 which 4 were shared by all three (Fig. 3D and data S3).

200

201 **FecB forms a complex with Rv3035 *in vitro***

202 To confirm the direct binding of Rv3035 and FecB *in vitro*, we cloned His-tagged Rv3035 from
203 *Mycobacterium thermoresistible* (Mth). Mth Rv3035 shares 67% sequence identity with Mtb
204 Rv3035 (fig. S4A) and was used because full-length or N-terminal truncation constructs of His-
205 tagged Mtb Rv3035 failed to yield soluble protein. Rv3035 is predicted to have an N-terminal
206 signal peptide by SignalP 6.0[14] and to be a lipoprotein, where the N-terminal cysteine residue is
207 predicted to form a thioether linkage to diacylglycerol[15,16]. Here, we have designated this N-
208 terminal cysteine as the first amino acid of the mature form of Rv3035 (fig. S4B). Our Mth Rv3035
209 protein construct begins at residue 2 of the predicted mature protein and was expressed with a
210 cleavable, N-terminal His-tag. Mth Rv3035-His was purified to homogeneity and the His-tag
211 cleaved, with size-exclusion chromatography (SEC) of the resulting protein suggesting that Mth
212 Rv3035 is monomeric (fig. S5A).

213 Mth Rv3035-His was also co-expressed with untagged Mtb FecB and found to co-elute by Ni-
214 affinity chromatography (fig. S5B). The Mth Rv3035 and Mtb FecB complex was stable during
215 SEC and displayed a molecular weight of 79.1 kDa, consistent with a heterodimer of Rv3035 and
216 FecB (fig. S5A). The affinity of Mth Rv3035 for Mtb FecB was quantified using isothermal titration
217 calorimetry (ITC). This analysis revealed tight 1:1 binding of Mth Rv3035 and Mtb FecB, with a
218 K_D of 27.5 $\pm$ 4.6 nM (Fig. 4A).

219

220 **Structure determination of Rv3035 and the FecB-Rv3035 complex**

221 We next solved the structure of Mth Rv3035 by X-ray crystallography to 1.9 Å (table S1). Mth
222 Rv3035 crystallized with two subunits in the asymmetric unit. In both subunits, there is clear
223 electron density for all but the N-terminal seven residues of Rv3035. The two subunits are virtually
224 identical with a root mean square deviation (rmsd) of 0.46 Å over 392 residues.

225 The structure of Rv3035 adopts a β-propeller fold, composed of eight 4-stranded β-sheets, where
226 each β-sheet is referred to as a blade (Fig. 4B and fig. S4A). At the N-terminus of the protein,
227 preceding the β-propeller fold, are ~40 residues that form an ordered loop region, which occupies
228 the bottom half of the central cavity formed by the β-propeller. A small portion of this N-terminal
229 region forms a β-strand (β_0, residues 27-32) that forms a β-sheet with the interior β-strand (β26)
230 of blade H (Fig. 4B and fig. S4A). The top half of the cavity is occupied by a second ordered loop
231 region formed by residues 171-197 containing a small α-helix (fig. S4A), which appears to act as
232 a cap (α-cap) for the central pore (Fig. 4B).

233 Mth Rv3035 contains two disulfide bonds (Fig. 4B, fig. S4A, and fig. S6A). The first is formed
234 between C71 and C87 and connects the exterior β-strand (β5) of blade B to the loop region on
235 the α-cap side of the β-propeller, and the second is formed between C187 and C194 connecting
236 the α-cap to the ordered loop region following it, perhaps stabilizing the cap region. A structural

homology search of Mth Rv3035 utilizing the DALI server[17] (table S2) demonstrated that the closest hits have extremely high structural homology with Rv3035 and the majority are accessory proteins that assist in remodeling protein assemblies; for example, two of the top hits are BamB from Gram-negative bacteria.

To determine the protein-protein interacting residues of the FecB-Rv3035 complex, we solved the X-ray crystal structure of the FecB-Rv3035 complex to a resolution of 3.35 Å (table S1). There are minimal structural differences between FecB alone[7] and FecB in complex with Rv3035 (fig. S6, C and D). One notable difference is the presence of a disulfide bond between C56 and C104 (fig. S6D), which is absent in the previous FecB crystal structure. Likewise, there are little differences between the structures of Rv3035 alone and in complex with FecB (fig. S6, E and F).

The FecB-Rv3035 complex interface is small and involves 729 $Å^2$ (5.6%) of the FecB surface, and 692 $Å^2$ (4.3%) of Rv3035 (Fig. 4C). Although the interface is small, there are multiple interactions between the two proteins including 19 hydrogen bonds and salt bridges that are $\leq$ 3.5 Å and six interactions that are < 3.0 Å (Fig. 4D and table S3). The interface involves residues from Rv3035 blade B (β4-β5) and residues from the loop that precedes blade B (between β1 and β2) (Fig. 4D and fig. S4A). The interface also involves the backbone nitrogen atom from disulfide bond forming C71 (Fig. 4D and fig. S6B). Strikingly, only nine Rv3035 residues are responsible for the polar interactions at the interface, with six residues forming multiple contacts with FecB: R43, K46, E77, R83, Q84, and R85, where R83 forms four polar contacts at the interface. FecB residues participating in the polar contacts at the interface are localized to the second lobe of FecB and are located in α7 (D223, H226), the loop between α8 and α9 (D258), the loop between α10B and β11 (A291, D292), and α13 (S320, R323, D324)[7]. Similar to Rv3035, several FecB residues are responsible for multiple contacts at the interface: H226, D292, S320, R323 and D324; where D292 forms five and D324 forms four polar contacts at the interface. The FecB-Rv3035 interface leaves the ligand binding site of FecB accessible to solvent, and thus still able to accommodate a ligand (Fig. 4C).

Key FecB residues in binding Rv3035

To test the functional importance of FecB residues involved in binding Rv3035, we mutated FecB D292 to alanine alone or H226, D292 and D324 to alanine together, and tested binding of these proteins to Rv3035 by protein interaction pull-down assays and by ITC. After determining that the mutants were properly folded by circular dichroism (fig. S7A), we utilized FecB-His and untagged Rv3035 in a nickel-affinity pull-down assay (fig. S7B). While WT FecB-His copurified with Rv3035, FecB D292A alone and the FecB triple mutant H226A_D292A_D324A failed to pull down Rv3035. In addition, no binding to Rv3035 was observed for the single and triple FecB mutants by ITC analysis (fig. S7C). Thus, the nanomolar affinity (K_D of ~30 nM) interaction between FecB and Rv3035 can be completely disrupted by mutating one FecB residue, D292.

Rv3035 mediates intrinsic multidrug resistance in Mtb

Having demonstrated that FecB and Rv3035 interact, we next set out to probe the cellular function of Rv3035. In TnSeq screens, *rv3035* mutants are usually annotated as having a "growth defect"[18] and are often absent from TnSeq screen input libraries. That is likely the reason why *rv3035* was not a hit in our TnSeq chemical-genetic interaction screen that identified *fecB* as important for intrinsic antibiotic resistance in Mtb[5]. Because *fecB* and *rv3035* display similar growth defects by CRISPRi[19], we reasoned that it would be possible to generate a *rv3035* knockout strain (Δ*rv3035*) to test directly whether Rv3035 mediates intrinsic resistance to different antibiotics. Although Δ*rv3035* colonies took longer to grow on agar plates than WT Mtb, the mutant strain exhibited similar growth kinetics as WT and Δ*fecB* in liquid media (fig. S8A). Additionally, we generated a Δ*fecB* Δ*rv3035* double knockout as well as the respective complemented mutants.

We performed MIC assays using these strains for several antibiotics having different mechanisms of action to which Δ*fecB* was hypersusceptible (Fig. 5A). Isoniazid was included as a control because its MIC is not affected by the absence of *fecB*. The single Δ*rv3035* and double Δ*fecB*Δ*rv3035* mutants showed very similar antibiotic hypersusceptibility patterns as Δ*fecB*, with reduced MICs compared to WT. As the basis for Δ*fecB*'s hypersusceptibility to antibiotics is likely a more permeable cell envelope compared to WT Mtb[5], we also tested whether Δ*rv3035* and Δ*fecB*Δ*rv3035* are more permeable to fluorescently labelled vancomycin and the reporter dye calcein-AM. Both mutants phenocopied Δ*fecB* with increased uptake of BODIPY-vancomycin (Fig. 5B) and both were hyperpermeable to calcein-AM similarly to Δ*fecB* (Fig. 5C).

Δ*fecB* also displayed altered colony morphology and a growth defect when growing as single colonies on agar plates, appearing smooth on high density spots and often failing to grow in lower spot dilutions (Fig. 5D). This makes experiments that rely on the quantification of Δ*fecB* colony forming unit (CFU) titers unreliable. Although we do not know the basis of this phenotype, it could be related to cell envelope alterations. Δ*rv3035* and Δ*fecB*Δ*rv3035* displayed the same defect (Fig. 5D). Taken together, these results demonstrate that Rv3035 is important for intrinsic multidrug resistance, mediates cell envelope impermeability and is required for regular growth on solid media. Importantly, deleting *fecB* and *rv3035* in the same strain did not result in enhanced phenotypes (Fig. 5, A-D), a result that it is expected for genes functioning in the same pathway.

To test whether binding between FecB and Rv3035 is required for maintaining cell envelope integrity, we complemented Δ*fecB* with an integrated plasmid expressing the FecB triple mutant H226A_D292A_D324A which fails to bind Rv3035 *in vitro* (fig. S7C). First, we confirmed that the FecB triple mutant is stably expressed *in vivo* (fig. S8B). Then, we tested whether Δ*fecB* complemented with the triple mutant (Δ*fecB*::*fecB*-H226A_D292A_D324A) can rescue Δ*fecB*'s hypersusceptibility to vancomycin and rifampicin. The MICs of these drugs were unchanged in Δ*fecB*::*fecB*-H226A_D292A_D324A compared to Δ*fecB* (Fig. 5E). Similarly, the FecB triple mutant failed to rescue Δ*fecB*'s growth defect in solid media (fig. S8C). These results indicate that FecB's binding to Rv3035 is critical to mediate intrinsic drug resistance in Mtb.

FecB and Rv3035 interact with cell envelope biosynthesis proteins

Our pull-down data revealed that FecB and Rv3035 also interact with the cell envelope biosynthesis proteins AftB and Rv0227c (Fig. 3, A and B), which was confirmed by co-

317 immunoprecipitation assays (fig. S9 and S10). Moreover, *fecB* and *rv3035* are co-essential with
318 *aftB* (Fig. 3C), which suggests they may perform similar functions and could be part of a protein
319 complex[12]. AftB catalyzes the last step in the biosynthesis of the arabinan domain of
320 arabinogalactan (AG) and lipoarabinomannan (LAM), adding the terminal arabinofuranose (Ara*f*)
321 residue to those molecules[20]. In AG, the β-(1 → 2)-linked terminal-Ara*f* residues provide mycolic
322 acid (MA) attachment sites which are critical for the formation of the mycolyl–arabinogalactan–
323 peptidoglycan (mAGP) complex[21,22]. Rv0227c (named polar growth factor A, or PgfA, in
324 *Mycobacterium smegmatis*) is an inner membrane protein that interacts with MmpL3, the
325 transporter for the cell envelope component trehalose monomycolate (TMM), and with a TMM
326 analog, suggesting that it participates in TMM transport across the plasma membrane[23].

327 In the periplasm, TMMs may donate a mycoloyl residue to AG to form the mAGP complex or to
328 another TMM molecule to form trehalose dimycolate (TDM or cord factor)[24]. While MAs attached
329 to AG (mAG) are the major components of the inner leaflet of the mycobacterial outer membrane
330 (MOM), TMMs, TDMs and free MAs are part of the outer leaflet of the MOM[3]. These lipids are
331 critical determinants of Mtb's cell envelope impermeability[3]. Since AftB and Rv0227c are involved
332 in the biosynthesis of mAG and the MOM, the interaction of FecB and Rv3035 with these proteins
333 suggests that they participate in the assembly or maintenance of mAG and/or the MOM.

334 We used AlphaFold 3[25] to predict the potential protein complexes formed by FecB, Rv3035, AftB
335 and/or Rv0227c, modeling different combinations of these proteins (fig. S11 and S12). The FecB
336 and Rv3035 complex showed a very high per-residue model confidence score (plDDT, fig. S11),
337 and has the same interface and orientation observed in the experimental structure of FecB-
338 Rv3035, superimposing with a rmsd of 0.91 Å over 696 residues (Fig. 4C). The complexes
339 containing AftB (with or without Rv0227c) showed a higher confidence score when modeled with
340 Rv3035 than with FecB alone (fig. S12, B and C). These structural models crossed the interface
341 predicted template modeling (ipTM) score threshold for high-quality prediction of 0.8 when AftB
342 was modelled with FecB and Rv3035, with Rv3035 and Rv0227c, or when all 4 proteins were
343 modeled together (fig. S12). This suggests that Rv3035 bridges the interaction between FecB and
344 AftB, and between FecB and Rv0227c.

345

346 **_AftB_ is more vulnerable to knockdown in Δ_fecB_ than in WT**

347 Because *aftB* shares an essentiality profile with *fecB* and *rv3035* (Fig. 3C), we decided to further
348 explore the genetic interaction between *fecB* and *aftB.* We depleted *aftB* with a weak CRISPRi
349 single guide RNA in both WT and Δ*fecB*. While this weak guide caused a slight growth defect in
350 WT upon induction of the CRISPRi system, knockdown of *aftB* by the same weak guide in Δ*fecB*
351 completely abrogated growth (Fig. 6A). This indicates that *aftB* is more vulnerable to knockdown
352 in Δ*fecB* than in WT as a moderate depletion of *aftB* leads to a profound loss of fitness in the
353 absence of *fecB*.

354

355 **FecB is required to maintain normal levels of MAs, TMMs and TDMs in Mtb**

356 To test whether FecB is required for proper assembly of the MOM, we performed lipidomics
357 analysis of total extractable lipids from WT, Δ*fecB* and Δ*fecB*::*fecB* strains (Fig. 6, B and E, and
358 data S4). Contrary to expectations that mycolate levels would be reduced in Δ*fecB* due to their
359 role in mediating envelope impermeability, the mutant displayed a higher abundance of TMMs
360 and free MAs compared to WT and Δ*fecB*::*fecB*.

361 Since TMMs accumulate in the plasma membrane of TMM transport mutants[23,26–28], we next
362 assessed if lipid trafficking was disrupted in Δ*fecB*. We treated bacterial pellets with the anionic
363 surfactant dioctylsulfosuccinate sodium (AOT) dissolved in heptane to strip non-covalently bound
364 lipids off the MOM[29]. In *Corynebacterium glutamicum*, AOT in heptane forms reverse micelles
365 which solubilize and capture OM surface lipids but does not penetrate other layers of the cell
366 envelope[29]. We validated this approach by analyzing known lipids extracted from the supernatants
367 and pellets of AOT treated samples, corresponding to the outer leaflet of the MOM (labelled OM)
368 and all other extractable lipids (labelled inner membrane or IM), respectively (fig. S13, A-D, and
369 data S4). Δ*fecB* displayed a higher abundance of TMMs and free MAs in both IM and OM
370 fractions, compared to WT and Δ*fecB*::*fecB* (Fig. 6, C-D and F-G, and data S4). We used the OM
371 fraction to visualize and quantify TDMs via thin-layer chromatography (Fig. 6H and fig. S13E).
372 Although TDM levels are inversely correlated with TMMs in mutants with defective TMM
373 transport[23,26–28], Δ*fecB* also displayed increased TDM levels compared to controls.

374 To validate the lipidomics data with an alternative method, we used the solvatochromic trehalose
375 probe DMN-Tre to track MA incorporation into TMMs via flow cytometry[30]. Upon entering the cell,
376 DMN-Tre is mycolylated to form DMN-Tre monomycolates, which are subsequently inserted into
377 the MOM, where the hydrophobic environment activates the probe's fluorescence[30].
378 Corroborating the lipid analysis, Δ*fecB* incorporated more DMN-Tre in its cell envelope than WT,
379 shown as increased mean fluorescence intensity compared to WT and Δ*fecB*::*fecB* (Fig. 6I), a
380 phenotype also shared with Δ*rv3035* (fig S13F).

381 Together, these results suggest that TMM transport occurs normally in Δ*fecB*, and the
382 accumulation of TMMs, TDMs and free MAs in the mutant is caused either by increased mycolate
383 lipid biosynthesis or blockage of a downstream process that uses these species as precursors,
384 such as incorporation of mycolic acids into mAG. Our RNA-seq data did not show differences in
385 transcript levels for MA/TMM biosynthesis genes in Δ*fecB* (data S1), thus favoring the second
386 hypothesis.

387 The *aftB* KD strains also displayed increased incorporation of DMN-Tre upon CRISPRi activation
388 (Fig. 6J). Since *aftB* directly controls the addition of mycolylation sites on AG, it is probable that
389 the *aftB* KD strain accumulates mycolates that do not attach to the cell wall[20,31] and the increased
390 incorporation of DMN-Tre reflects the redirection of the mycolate pool towards the MOM.

391

392 **FecB is essential for virulence of Mtb in mice**

393 The mycobacterial cell envelope is a formidable barrier that protects Mtb not only from antibiotics
394 but also from host immune responses[3]. Thus, we hypothesized that *fecB* might also be required
395 for Mtb to establish a successful infection in mice. The unreliability of Δ*fecB* to grow as single

396 colonies on agar plates (Fig. 5D), however, impairs the quantification of the bacterial burden in
397 infected mice. To circumvent this problem, we implemented a genetic switch to activate *fecB*'s
398 expression in the presence of a tetracycline inducer (TetON)[32] and allow quantification of CFUs
399 from mice infected with Δ*fecB* harboring the TetON switch (FecB-TetON). The conditional
400 expression of *fecB* was validated via MIC assays with vancomycin and rifampicin, which showed
401 that addition of ATc rescued the antibiotic hypersusceptibility of FecB-TetON (Fig. 7A).

402 Mice were infected via the aerosol route with FecB-TetON and received either regular or
403 doxycycline (doxy) chow throughout the course of the experiment (Fig. 7, B and C). Lung and
404 spleen homogenates from both groups were cultured on agar containing ATc to activate *fecB*
405 expression *ex vivo*. FecB-TetON grew and established a high titer chronic infection in the lungs
406 of mice fed with doxy-containing chow (Fig. 7B). In contrast, in mice receiving regular chow, FecB-
407 TetON grew during the first 14 days post-infection (p.i.), after which CFU counts remained
408 relatively stable for another 8 weeks p.i. Dissemination to the spleen was delayed, and similarly
409 to the lung, spleen bacterial burden was significantly lower in mice receiving regular versus doxy
410 chow (Fig. 7C). Thus, we conclude that *fecB* is required for Mtb virulence and plays a critical role
411 during growth in the acute phase of infection but is not required for Mtb's persistence in the host.

412

413 **Discussion**

414 The mycobacterial cell wall, comprised of peptidoglycan, arabinogalactan and mycolic acids, has
415 been a key target of several anti-TB drugs[33]. Two of the four first-line TB drugs, isoniazid and
416 ethambutol, target mycolic acid and arabinogalactan biosynthesis, for instance. Although these
417 drugs were developed more than 60 years ago, they remain part of the standard TB chemotherapy
418 due to their success in treating drug-susceptible Mtb infections, which validates efforts to explore
419 novel inhibitors that target the cell wall of Mtb[10]. Despite being an important target for drug
420 development and playing a central role in Mtb pathogenesis and intrinsic drug resistance, many
421 aspects of the Mtb cell wall, and more broadly, cell envelope, such as assembly and maintenance
422 remain unknown. In the current study, we describe two periplasmic proteins, FecB and Rv3035,
423 that work together to mediate cell envelope impermeability and intrinsic multidrug resistance in
424 Mtb.

425 Our transcriptomic data indicate that Mtb lacking *fecB* upregulates the *iniBAC* operon (**i**so**n**iazid
426 **i**nduced genes B, A and C), which is named for being induced by isoniazid, ethambutol, and other
427 inhibitors of cell wall biosynthesis[10]. Upregulation of the *iniBAC* genes in Δ*fecB* occurred
428 independently of the presence of detergent in the media and most likely reflects a constitutive
429 defect in cell wall integrity, which results in Δ*fecB's* increased membrane permeability[5].

430 The iron-deprivation transcriptional signature and accumulation of siderophores in Δ*fecB* grown
431 in detergent-free media points to *fecB* having an activity in iron homeostasis. However, whether
432 this is a direct or indirect effect remains unclear. While FecB can bind ferric-carboxymycobactin
433 with high affinity *in vitro*[7], experiments probing the requirement of *fecB* for iron acquisition *in vivo*
434 showed only minor growth phenotypes (Fig. 1D and fig. S1B). FecB variants with lower binding
435 affinity to ferric-carboxymycobactin (FecB E339S_R240S and E339S_Y242S) rescued the iron-
436 deprivation transcriptional signature and slower growth of Δ*fecB* in iron-limiting conditions,

437 suggesting that binding to iron-loaded siderophores is dispensable in FecB's ability to reverse
438 those phenotypes. On the other hand, FecB E339S_R240S and E339S_Y242S have slightly
439 higher binding affinity to apo-carboxymycobactin and thus we could not test the *in vivo*
440 requirement of FecB's binding to iron-free apo-siderophores using these variants. Importantly,
441 using FecB E339S_R240S and E339S_Y242S, and other genetic and microbiological
442 approaches, we showed that FecB's role in iron homeostasis is likely not connected to its role in
443 mediating antibiotic resistance in Mtb.

444 Specific evidence for FecB's function in cell envelope integrity came to light upon identification of
445 FecB's most enriched physical interactors: Rv3035, AftB and Rv0227c. In *Mycobacterium*
446 *marinum*, FecB was also found to interact with AftB and the Rv3035 homologue MMAR_1667[34].
447 Although AftB's function has been well described in the literature[20,35,36], only a few studies explore
448 the function of Rv0227c[23,37] and Rv3035[34] homologues in mycobacteria. Here we report on the
449 structure of Rv3035 alone and the FecB-Rv3035 complex, which identified key FecB residues
450 involved in binding Rv3035 that we were able to validate. Moreover, we show that FecB's binding
451 to Rv3035 is required for its function in mediating antibiotic resistance in Mtb. Mtb∆*rv3035* and
452 the double knockout ∆*fecB*∆*rv3035* displayed the same phenotypes indicative of perturbed cell
453 envelope integrity as ∆*fecB*. This indicates that the absence of either protein equally impacts the
454 function of the complex and thus both are required to fulfill their function.

455 Structural homology analysis for Rv3035 revealed two classifications of structural homologs (table
456 S2). One class represents assembly factors that contribute to scaffolding in larger complexes,
457 facilitating the coordinated movement of multiple protein components. This includes BamB of the
458 prokaryotic β-barrel assembly machinery (BAM) complex, and the eukaryotic ODA16, an
459 assembly factor involved in outer dynein arm intraflagellar transport[38]. When comparing these
460 structural homologs to Rv3035, both the N-terminal propeller cavity plug region and the α-cap
461 present in Rv3035 are absent in these assembly factors. The second class of Rv3035 structural
462 homologs have enzymatic activity. Strikingly, these structural homologs - *Acidithiobacillus*
463 *ferrooxidans* tetrathionate hydrolase[39], *Methylacidiphilum fumariolicum* SolV methanol
464 dehydrogenase[40], and the *Devosia albogilva* quinone-dependent dehydrogenase[41] - all have
465 secondary structure elements similar to the Rv3035 α-cap and bear an N-terminal propeller
466 central cavity plug. However, in these enzymatic structural homologs, the propeller fold is more
467 extensively decorated than in Rv3035. Indeed, Rv3035—due to the presence of N-terminal
468 propeller cavity plug and the propeller decorations—has greater similarity with its enzymatic
469 structural homologs than the assembly factor homologs. Although our studies show that Rv3035
470 acts as a scaffolding protein in its interactions with FecB, its resemblance to the enzymatic
471 homologs raises the possibility that Rv3035 may possess an as-yet unidentified enzymatic
472 activity.

473 What is the function of FecB and Rv3035? And how do these proteins contribute to intrinsic
474 multidrug resistance in Mtb? Our initial attempts at answering these questions point to FecB's and
475 Rv3035's interaction with AftB. Corroborating our proteomics dataset, the genes encoding FecB,
476 Rv3035 and AftB share CRISPRi essentiality profiles, and AlphaFold 3 predicts a very high
477 confidence model of the complex formed by the three proteins. In this model, Rv3035 bridges the
478 interaction of FecB and AftB, and the two periplasmic proteins are positioned in close proximity to

479 AftB's active site cavity[42]. The proposed orientation suggests that the FecB-Rv3035 complex
480 could serve as scaffold for AftB's attachment to its substrate AG or play a role in controlling AftB's
481 arabinofuranosyltransferase activity. If one of these hypotheses is correct, one would expect
482 reduced terminal arabinofuranose residues (mycolylation sites) on AG and, consequently, lower
483 levels of MA covalently attached to AG which would compromise the structure and integrity of the
484 cell wall[35]. A decreased ratio of arabinose to galactose in AG was observed in a *M. marinum fecB*
485 mutant, supporting the hypothesis that FecB influences AftB's function[34]. Additionally, an
486 impairment of AftB's function leads to production of a truncated LAM that is pro-inflammatory[20]
487 and can also influence cell envelope integrity[34,43].

488 Our lipidomics dataset further supports the hypothesis that FecB participates in AftB's function as
489 the increased levels of TMMs, TDMs and free MAs observed in Δ*fecB* could be a direct
490 consequence of reduced attachment of MAs to the cell wall (fig. S14). This phenotype is observed
491 in Mtb treated with ethambutol[44] (inhibitor of AG biosynthesis), and in deletion mutants of *aftB*[20]
492 and *aftC*[31] (another arabinofuranosyltransferase) in *C. glutamicum* and *M. smegmatis*,
493 respectively, which all show increased levels of trehalose mycolates. Finally, while Δ*fecB*, Δ*rv3035*
494 and *aftB* KD strains showed similar increased incorporation of DMN-Tre into the MOM, this
495 phenotype was enhanced when *aftB* was selectively depleted in Δ*fecB* (Fig. 6J). Moreover, such
496 depletion also completely inhibited the growth of Δ*fecB* (Fig. 6A). This indicates that residual
497 AftB's activity remains in Δ*fecB* and further disruption of mycolate turnover is possible by targeting
498 *aftB* in the absence of *fecB*. Based on this, we posit that FecB, and by extent Rv3035, support
499 but are not essential for AftB's arabinofuranosyltransferase activity *in vivo*. This new
500 understanding of the requirements for cell envelope integrity in Mtb can be used to inform future
501 TB drug discovery efforts.

502

503 **Materials and Methods**

504

505 **Bacterial strains and culture conditions**

506 Mtb strains used in this study are listed in data S5. For most experiments, the strains were cultured
507 in Middlebrook 7H9 medium (BD, #271310) supplemented with 0.2% glycerol, 0.5% bovine serum
508 albumin fraction V, 0.2% dextrose, 0.085% NaCl and 0.05% Tween80 (Sigma, # P8074), this is
509 referred to as "regular" medium. For detergent-free conditions, Tween80 was omitted from the
510 media recipe. For growth in iron-limiting conditions, self-made 7H9 medium without ammonium
511 ferric citrate (AFC) was prepared and chelated for 2 days with 20g/liter of BioRad Chelex 100
512 resin. After filter-sterilization, metals other than iron were added according to their concentrations
513 in Middlebrook 7H9. To prepare Low/High Iron media, 1μM or 160μM of AFC was added to iron-
514 chelated medium, respectively. For reference, Middlebrook 7H9 medium contains 150μM AFC.
515 Where required, antibiotics or small molecules were used at the following concentrations:
516 hygromycin (50μg·ml^{-1}), kanamycin (25μg·ml^{-1}), zeocin (25μg·ml^{-1}), streptomycin (25μg·ml^{-1}),
517 apramycin (60μg·ml^{-1}) and ATc (200ng·ml^{-1} for CRISPRi strains and 1000ng·ml^{-1} for FecB-
518 TetON). The strains were grown at 37°C and 5% CO_2 in a standing incubator, unless otherwise
519 indicated.

520

521 **Plasmids construction**

522 Plasmids used in Mtb strains are listed under the strain “full name” after the double colon in data
523 S5. Plasmids starting with pGM were constructed using Invitrogen Gateway Cloning system.
524 Constructs harboring the gene of interest were synthesized by GenScript. CRISPRi constructs
525 were generated as previously described[19].

526

527 **RNA extraction**

528 Total RNA was extracted from 10mL of mid-log phase bacterial cultures by first adding 1:1
529 guanidinium thiocyanate buffer followed by centrifugation for 10 minutes at 4°C. Bacterial pellets
530 were bead-beaten into 0.9mL Trizol, 0.2mL chloroform was added to each sample and RNA in the
531 aqueous phase was purified using the RNA Clean and Concentrator-25 kit (Zymo Research
532 #R1017). After elution, samples were incubated with TURBO DNase (Ambion, AM2238) at 37°C
533 for 1h to remove residual genomic DNA. Samples were then repurified using the RNA Clean and
534 Concentrator-25 kit or RNA Clean and Concentrator-5 kit (Zymo Research #R1015).

535

536 **RNA-sequencing (RNA-seq) and analysis**

537 Ribosomal RNA (rRNA) was removed from total RNA as previously described[45]. The resulting
538 rRNA-depleted RNA was then concentrated with the RNA Clean and Concentrator-5 kit (Zymo
539 Research #R1015). RNA-seq libraries were created from these samples using the NEBNext Ultra
540 II Directional RNA Library Prep Kit for Illumina (New England Biolabs, E7760L) along with
541 NEBNext Multiplex Oligos for indexing (New England Biolabs). The libraries were purified using
542 Dynabeads MyOne Streptavidin C1 (Thermo Fisher #65002), assessed for quality with a
543 Bioanalyzer, and pooled based on their unique indexes. Sequencing was carried out on an
544 Illumina NextSeq2000 platform at the Genomics Resources Core Facility of Weill Cornell
545 Medicine.

546 RNA-seq data analysis was conducted using R. Sequencing reads underwent trimming and
547 filtering with Rfastp, followed by alignment to the H37Rv reference genome (GenBank
548 AL123456.3; RefSeq NC_000962.3; GCF_000195955.2; Genome assembly ASM19595v2) using
549 the Rsubread package[46,47]. BAM alignment files were generated, sorted, and indexed using
550 Rsamtools. Read quantification was carried out with featureCounts, and differential gene
551 expression analysis was performed using DESeq2[48,49].

552

553 **Lipid extraction**

554 Mtb cultures were grown in detergent-free 7H9 containing fatty acid-free BSA until mid-log phase.
555 Bacterial pellets were transferred to sterile filters[50] which were added directly to 16 x 100mm glass
556 tubes containing 2:1 chloroform: methanol or to 2mL screw cap tubes containing 1mL of 10mM

557 AOT dissolved in heptane or PBS as a control. For AOT treatment, pellets in AOT or PBS were
558 agitated in a bead-beater at low speed (2800rpm) for 10s to knock the cells off the filters followed
559 by removal of filters and incubation in a cooling rack for 1h, with mixing by inversion of the tubes
560 every 5 minutes. 500µL of AOT supernatant was added to 16 x 100mm glass tubes containing
561 2:1 chloroform: methanol. AOT and PBS pellets were resuspended in 600µL of 2:1 chloroform:
562 methanol and added to 16 x 100mm glass tubes containing 2:1 chloroform: methanol.

563

564 **Liquid chromatography-mass spectrometry (LC-MS) analysis**

565 Lipid extracts were centrifuged at 4000rpm for 15 minutes at 4°C and the supernatant decanted
566 into new 16 x 100mm borosilicate tubes. The tubes were dried using a GeneVac evaporator under
567 vacuum with gentle heating to 40°C. The residual residue was transferred to pre-weighed 4mL
568 amber vials using 2mL 1:1 chloroform: methanol. The solution was again dried using the GeneVac
569 evaporator. The vials were re-weighed to obtain the dry weight of lipid extract, and this mass was
570 used to prepare a 1mg/mL solution in 1:1 chloroform: methanol. Lipids were stored at -20°C as a
571 stock solution. A 150µL aliquot of stock solution was transferred to a glass insert tube (250µL,
572 Agilent Technologies) nested within a microfuge tube. The aliquot was evaporated to dryness
573 using an argon air stream then resuspended in 150µL of a solution of 70% hexanes and 30%
574 isopropyl alcohol. After briefly vortexing to resuspend, the samples were centrifuged at 4000rpm
575 for 15 minutes at 4°C. A volume of 100µL of the supernatant was transferred to a 2mL amber vial
576 (Agilent) equipped with 250µL glass insert tubes and capped with 9mm septum-embedded screw
577 caps (Agilent). A 10µL injection of this sample was analyzed using liquid chromatography mass
578 spectrometry (LC-MS) on an Agilent 6520 ESI-QTOF. Separation of lipids using a 3µm diol column
579 (2.1 x 150mm) and gradient elution from solvent A (70% hexane, 30% isopropanol, .02% formic
580 acid, .01% ammonium hydroxide) to solvent B (70% isopropanol, 30% methanol, .02% formic
581 acid, .01% ammonium hydroxide) as previously described[51]. Following chromatography, the
582 sample underwent electrospray ionization at 325°C with 5 L/min drying gas flow at 5500 V and
583 30 psig nebulizer pressure and ions were detected by time-of-flight in both positive and negative
584 modes (m/z range: 100 – 3000). Internal calibrants (922.009798 positive mode, 983.0325
585 negative mode) were infused continuously.

586 Lipids were identified using unique mass-retention time identifiers for masses exhibiting the
587 expected isotopic distributions as previously reported[51]. Integrations of ion abundance were
588 determined using Agilent Profinder 8.0 and Qualitative Analysis 6.0.

589

590 **Growth curves**

591 Mtb strains were inoculated from frozen glycerol stocks and grown with appropriate selection
592 antibiotics in 7H9 medium until mid-log phase at 37°C.

593 For pre-depletion of iron internal stores, bacteria were washed in PBS or iron-chelated 7H9 and
594 diluted to an OD_{580nm} of 0.05 in iron-chelated 7H9. After 4-5 generations, bacteria were spun down
595 at 800rpm for 8 minutes to generate a single cell suspension. Bacteria were diluted to an OD_{580nm}

596 of 0.025 in the indicated media and added to flasks which were incubated standing at 37°C. For
597 serial passaging, when cultures in high iron media reached stationary phase, low iron cultures
598 were spun down at 800rpm for 8 minutes to generate a single cell suspension and bacteria were
599 diluted to an OD_{580nm} of 0.025 in both high/low iron media. OD measurements from cultures in
600 flasks were performed in a spectrophotometer. For growth curves in low iron media without
601 detergent, iron pre-depleted cultures were washed in PBS or detergent-free iron-chelated 7H9,
602 diluted to an OD_{580nm} of 0.05 and 100µL of bacteria were added to a 96-well plate in triplicates.
603 OD measurements from plates were performed in a plate reader. Cultures grown in 96-well plates
604 were resuspended prior to OD_{580nm} readings.

605 For CRISPRi strains, cultures were split into two flasks and 200ng/mL of ATc added to one of the
606 flasks 2-3 days prior to setting up the growth curve to pre-deplete the gene of interest. Fresh ATc
607 (200ng/mL) was again added to the media (+ATc conditions) before distributing bacteria into
608 96/384-well plates in triplicates.

609

610 **Reverse transcription quantitative polymerase chain reaction (RT qPCR)**

611 Primers and probes for RT qPCR are listed in table S4. Primers and probes were ordered from
612 TIB MOLBIO, LLC. cDNA was generated using MluV reverse transcriptase (New England Biolabs)
613 and approximately 500ng of total RNA. Parallel no-reverse transcriptase reactions were prepared
614 as a control for residual genomic DNA. qPCR was performed in the LightCycler® 480 System
615 (Roche). The housekeeping gene *sigA* (Rv2703) was used as an internal control. *sigA* probes
616 were labeled with 5' LC760/3' BBQ. Probes targeting genes of interest were all labeled with 5'
617 6FAM/3' BBQ or 3' BHQ.

618

619 **Minimal inhibitory concentrations (MIC) assays**

620 Mtb strains were inoculated from frozen glycerol stocks and grown with appropriate selection
621 antibiotics in 7H9 medium until mid-log phase at 37°C. Bacteria were diluted to an OD_{580nm} of 0.01
622 in 7H9 and 50µL of bacteria were added to a 384-well plate in triplicates per antibiotic
623 concentration, or to triplicate control wells without antibiotics. The HP D300e digital dispenser was
624 used to deliver antibiotics to plate wells. Bacteria were grown in standing cultures at 37°C and
625 OD_{580nm} was measured in a plate reader between days 10-21 following treatment (time point is
626 indicated in each figure legend). For MICs in low iron or detergent-free conditions, bacterial
627 cultures were first washed in PBS once or twice prior to dilution into the respective media of the
628 MIC assay. For CRISPRi strains, cultures were split into two flasks and 200ng/mL of ATc added
629 to one of the flasks 2-3 days prior to setting up the MIC assay to pre-deplete the gene of interest.
630 Fresh ATc (200ng/mL) was again added to the media of the assay (+ATc conditions) before
631 distributing bacteria into plates.

632

633 **Pull-down tandem mass spectrometry**

634 *Sample preparation*

635 Whole-cell lysates were collected from log-phase cultures grown in the shaking incubator,
636 incubated with 1% n-dodecyl -D-maltoside for 2h on a rotator at 4°C, followed by incubation with
637 anti-DYKDDDDK (FLAG) magnetic agarose (Pierce #A36797). Captured proteins were
638 dissociated from magnetic agarose by addition of 3x DYKDDDDK (3xFLAG) peptide (Pierce
639 #A36805), according to the manufacturer's instructions. Sodium Dodecyl Sulfate (SDS) was
640 added to the peptide eluate at a final concentration of 2% and samples were boiled at 95°C for
641 10 minutes. Boiled samples were transferred to protein lo-bind tubes. FLAG- (or 3xFLAG-) tagged
642 bait proteins were detected in eluates on an SDS-Polyacrylamide Gel Electrophoresis (PAGE) gel
643 prior to mass spectrometry.

644 23µg of proteins per sample were flash frozen on dry ice and subsequently dried using a Speed-
645 Vac. Next, 23µl of lysis buffer (5% SDS, 50mM TEAB) was added to initiate the S-Trap™ Micro
646 Spin digestion protocol (PROTIFI). The proteins underwent reduction by 4mM dithiothreitol (DTT)
647 and alkylation by 20mM iodoacetamide. Following an overnight digestion with trypsin at 37 °C,
648 peptides were eluted first by addition of 40µL of 50mM triethylammonium bicarbonate (TEAB) and
649 spun at 4000 rpm for 1 min. This was followed by a 1-minute spin with 40µL of 0.2% formic acid
650 (FA) and, lastly, 40µL of 50% acetonitrile (ACN). The three elution were then pooled together,
651 dried using a Speed-Vac, and reconstituted in 20µL of 0.1% FA in 5% ACN. After reconstitution,
652 the samples were centrifuged at 16,000 rpm for 16 min and an 18µL aliquot of the supernatant
653 was transferred to a non-binding HPLC vials.

654

655 *LC-MS/MS and data analysis workflows*

656 Data from the first experiment (pull-down of FecB-FLAG) was acquired on a TimsTOF Pro2
657 (Bruker) mass spectrometer, which was coupled to a nanoElute LC system from Bruker. 5µL of
658 peptides were loaded and separated on an in-house 75 µm I.D. fused silica analytical column
659 packed with 25-cm ReproSil-Pur C18-AQ (Dr. Maisch, GmbH, 120 Å, 3 µm) particles to a gravity-
660 pulled tip, using an aqueous mobile phase (A) of water and 0.1% FA and an organic mobile phase
661 (B) of ACN and 0.1% FA. A 30-minute gradient was employed for DDA-PASEF with a flow rate
662 set at 500 nL/min. The captive nano-electrospray voltage was maintained at 1600V, using one
663 column configuration (no trap). The DDA-PASEF method consists of 10 MS/MS PASEF scans per
664 topN acquisition cycle, with ramp and accumulation times of 100 ms, covering an m/z range from
665 100 to 1700 and an ion mobility range (1/K0) from 0.70 to 1.30 V s/cm^2. Collision energy settings
666 followed a linear function of ion mobility, ranging from 20 eV at 0.6 V s/cm^2 to 59 eV at 1.6 V
667 s/cm^2, using default parameters. Calibration of the instrument was performed using three ions
668 from the ESI-L Tuning Mix (Agilent) (m/z 622, 922, 1222).

669 The custom workflow 'LFQ-MBR' from FragPipe version 21.1 was used, including database
670 search with MSFragger (version 4.0), deep-learning prediction rescoring with MSBooster,
671 Percolator and ProteinProphet (Philosopher version 5.1.0) for PSM validation and protein
672 inference. The raw files from TimsTOF Pro2 were searched against the database
673 "Mycobacterium_tuberculosis_H37Rv_v4modified" appended with common contaminant
674 proteins. Decoy reversed sequences were appended to the search database. The default

675 MSFragger search parameters were used, except precursor and fragment mass tolerances were
676 set to 20 ppm; enzyme: trypsin (not cutting before P); peptide length 7-30. Variable modifications
677 were set to oxidation of Met and acetylation of protein N-t, and fixed modifications to
678 carbamidomethylation of Cys. MSBooster, Percolator and ProteinProphet default options were
679 used, and results were filtered by 1% FDR at protein level. The searched results were then
680 imported to Scaffold 5 Q+S (Proteome Software Inc., v5.3) for data visualization.

681 Data from the second experiment (pull-down of Rv3035-3xFLAG) was acquired using a
682 NanoAcquity UPLC (Waters Corporation, Milford, MA) coupled to an Orbitrap Fusion Lumos
683 Tribrid (Thermo Fisher Scientific, Waltham, MA) mass spectrometer. Peptides were trapped and
684 separated using an in-house packed precolumn packed with 2cm ReproSil-Pur C18-AQ (Dr.
685 Maisch, GmbH, 120 Å, 5 µm) particles plus and an in-house 75 µm I.D. fused silica analytical
686 column (as previously described) and the same solvent composition. 3.8µL sample was injected,
687 and the peptides were trapped at a flow rate of 4µL/min with 5% mobile phase B for 4 min, followed
688 by a gradient elution with 5-35% B at a flow rate of 300nL/min over 120 min (total run time 145
689 min). Mass spectra were acquired over m/z 375-1500 Da with a resolution of 120,000 (m/z 200).
690 Tandem mass spectra were acquired using data-dependent acquisition with an isolation width of
691 1.6 Da, HCD collision energy of 30%, resolution of 15,000 (m/z 200), maximum injection time of
692 50 ms, and an AGC target of 50,000.

693 Raw data files from the Orbitrap Fusion Lumos Tribrid were peak processed with Proteome
694 Discoverer (version 2.5, Thermo Scientific) followed by identification using Mascot Server (Matrix
695 Science, v2.6.2) against the same database used in the previous experiment. Search parameters
696 were as follows: tryptic digestion with up to 2 missed cleavages; peptide N-terminal acetylation,
697 methionine oxidation, and N-terminal glutamine to pyroglutamate conversion were specified as
698 variable modifications. Carbamidomethylation of cysteines was set as static modification.
699 Assignments were made using a 10-ppm mass tolerance for the precursor and 0.6 Da mass
700 tolerance for the fragment ions. All non-filtered search results were processed by Scaffold 5 Q+S
701 at 1.0% false-discovery rate (FDR) for peptides and 99% threshold for proteins (2 peptides
702 minimum).

703 For each experiment, Total Spectrum Count (TSC) was exported from Scaffold 5 Q+S into a
704 Microsoft Excel spreadsheet. Zeros were replaced with ones in WT control samples to allow fold-
705 change (FC) calculation of every protein detected in the samples containing the bait protein. For
706 normalization, we summed the TSC values for all proteins in each replicate, calculated the
707 average of the sum of the three replicates and divided the average by the sum value of each
708 replicate (this is the normalization factor). Then, we multiplied each protein TSC by the
709 normalization factor of that replicate sample, calculated the median, log2FC of tagged group over
710 WT control, and p-value by performing T-tests of the normalized values in each row. P-values
711 were transformed into -log10(p-value) for visualization of the data as a volcano plot.

712

713 **Co-essentiality analysis**

714 We performed co-essentiality analysis on CRISPR interference (CRISPRi) data from Li, Poulton
715 *et al.*[13], which profiled Mtb fitness under 80 experimental conditions. These conditions span 9

716 antibiotics (BDQ = bedaquiline; CLR = clarithromycin; EMB = ethambutol; INH = isoniazid;
717 LVX = levofloxacin; LZD = linezolid; RIF = rifampicin, STR = streptomycin; VAN = vancomycin),
718 each tested under 9 screening conditions defined by a combination of pre-depletion time (1, 5, or
719 10 days of CRISPRi induction before drug exposure) and drug concentration ("Low," "Medium,"
720 or "High" partially inhibitory doses). We used only the $\log_2$ fold change (LFC) values from negative
721 selection screens, which report the fitness effects of gene knockdown.

722 Each gene was thus represented by an 80-dimensional LFC vector capturing its essentiality
723 profile across the drug/time/concentration matrix. To account for covariance across screens—
724 such as batch effects—we computed an 80 × 80 empirical covariance matrix (Σ) from the LFC
725 data. We then applied generalized least squares (GLS), following the approach of Wainberg *et*
726 *al.*[52] to compute pairwise co-essentiality relationships among 3,979 genes. This yielded a 3,979
727 × 3,979 matrix of GLS coefficients and corresponding p-values.

728 We corrected for multiple hypothesis testing using the Benjamini–Hochberg procedure
729 (fdrcorrection in the Python statsmodels package). Gene pairs with a false discovery rate (FDR)-
730 adjusted p-value < 0.001 were considered significantly co-essential, resulting in approximately
731 16,000 high-confidence gene pairs.

732

733 **Design of expression constructs for *M. thermoresistibile* (Mth) Rv3035**

734 Initial attempts to express Mtb Rv3035 in *E. coli* using N- or C-terminal 6xHis-tag (His) constructs
735 with full-length and various N-termini truncations failed to produce soluble Rv3035. To improve
736 solubility, we turned to a thermostable homolog of Rv3035, Mth Rv3035, Accession no.
737 WP_040546537, and constructed two *E. coli* codon-optimized constructs cloned into pET28a with
738 a TEV-cleavable N-terminal His-tag (GenScript, Piscataway, NJ). The Mth Rv3035 construct that
739 encodes for the mature form of Rv3035 without its predicted signal peptide (SignalP 6.0[14]) and
740 starts at residue Gly2 (fig. S4B), produced soluble Rv3035 only when expressed in *E. coli*
741 T7SHuffle cells (New England Biolabs, Ipswich, MA). Notably, T7SHuffle cells promote disulfide
742 bond formation[53], and Rv3035 is predicted to harbor two disulfide bonds.

743

744 **Generation of FecB mutants for *in vitro* studies**

745 A pET28a FecB construct encoding Mtb FecB (without the signal peptide, mature FecB starting
746 at residue 39) with a thrombin-cleavable N-terminal 6xHis-tag[7] was used as the template for *in*
747 *vitro* site-directed mutagenesis using Pfu Ultra Fusion HS DNA polymerase (Agilent) with the
748 primers listed in table S5 and then confirmed by DNA sequencing (GeneWiz from Azenta Life
749 Sciences). The FecB construct encoding no His-tag was generated by using the pET28a FecB
750 plasmid and excising the encoded *fecB* gene with *Nde*I and *BamH*I and ligating it into a pET22b
751 vector.

752

753 **Expression and purification of Mth Rv3035 and the Mth Rv3035-Mtb FecB complex**

754 Mth Rv3035-His was expressed in *E. coli* T7SHuffle cells in Terrific Broth (TB) media containing
755 0.4% glycerol and 50µg/mL kanamycin (Kan). To express the Mth Rv3035-Mtb FecB complex,
756 which we refer to as the FecB-Rv3035 complex throughout the manuscript, both pET28a Mth
757 Rv3035-His and pET22b Mtb FecB plasmids were co-transformed into T7SHuffle cells with
758 selection on LB + 50µg /mL Kan and 100µg/mL ampicillin (Amp) agar plates. A fresh transformant
759 was used to inoculate TB containing 0.4% glycerol, 50µg/mL Kan and 100µg/mL Amp. Cells were
760 grown at 37°C to an OD_{600nm} of ~ 0.6, before protein expression was induced by the addition of
761 0.5mM isopropyl β-D-1-thiogalactopyranoside (IPTG). The cells grown overnight at 20°C and
762 harvested by centrifugation.

763 Both Mth Rv3035-His and the FecB-Rv3035-His complex were purified using the same protocol.
764 Cell pellets were resuspended in 10x vol(mL)/w(g)of cells in Buffer A (150mM NaCl, 50mM Tris,
765 pH 7.8) with 0.25mM phenylmethylsulfonyl fluoride (PMSF) with stirring at 4°C for 30 minutes.
766 Cells were lysed by sonication and cell debris was pelleted by centrifugation at 14,000rpm for 1h
767 at 4°C. The cell lysate was passed through a 1µm syringe filter to remove insoluble debris and
768 applied to a His-trap column (Cytiva, Marlborough, MA) pre-equilibrated with Buffer A using an
769 AKTA Start FPLC instrument (Cytiva, Marlborough, MA). Following a 10x column volume (CV)
770 wash step with Buffer A, a gradient of Buffer A from 0 to 500mM imidazole over 20 CVs elute His-
771 tagged proteins. Fractions with containing Mth Rv3035-His or the FecB-Rv3035-His complex
772 were concentrated using an Amicon concentrator (MilliporeSigma, 30kDa cut-off) with buffer
773 exchange into Buffer A.

774

775 **Expression and purification of Mtb FecB and mutants**

776 Purification of WT FecB and FecB mutant proteins were carried out in a similar manner as
777 previously described[7]. FecB WT or mutants were expressed in BL21-(DE3) cells and cells were
778 grown in TB + 0.4% glycerol + 50µg/mL kanamycin at 37°C to an OD_{600nm} of ~0.6, before protein
779 expression was induced with IPTG (0.5mM). Cell growth was continued overnight for 20h at 20°C,
780 before cells were harvested by centrifugation. Cell pellets were resuspended in 10x vol(mL)/w(g)
781 Buffer B (350 mM NaCl, 50 mM Tris, pH 7.8, 10% glycerol) with 0.25mM PMSF with stirring at
782 4°C for 30 minutes. Cells were lysed by sonication and cell debris was pelleted by centrifugation
783 at 14,000rpm for 1h at 4°C. The cell lysate was filtered and applied to a Ni-NTA resin pre-
784 equilibrated with Buffer B using gravity flow. The column was washed with Buffer B and eluted
785 with a stepwise elution gradient of imidazole going up to 600mM imidazole in Buffer B. Fractions
786 found to contain FecB by SDS-PAGE analysis (expected MW ~37 kDa) were pooled and dialyzed
787 against Buffer B overnight at 4°C.

788

789 **Removal of N-terminal His-tag from Rv3035-His and FecB-His**

790 For cleavage of His-tags from Rv3035-His and from the FecB-Rv3035-His complex, TEV was
791 added to approximately 30-100mg of protein at a final concentration ~0.1mg/ml TEV and
792 incubated overnight at 4°C. The cleavage reaction was passed over a Ni-NTA column pre-
793 equilibrated with Buffer A + 10mM imidazole and chased with Buffer A + 10mM imidazole. Flow-

through fractions containing Rv3035 or FecB-Rv3035 complex were concentrated and buffer exchanged into Buffer A.

For the isolation of tag-free WT FecB, which was used for some ITC experiments, a similar procedure was used but with thrombin at ~30U thrombin:1mg FecB-His. The cleavage reaction was passed over a Ni-NTA column pre-equilibrated with Buffer B + 10mM imidazole and chased with Buffer B + 10mM imidazole. Flow-through fractions containing WT FecB were concentrated and buffer exchanged into Buffer B.

Isothermal titration calorimetry (ITC) experiments

ITC experiments were carried out using a Malvern MicroCal PEAQ-ITC instrument (Malvern, United Kingdom). Prior to the experiments, proteins were dialyzed into Buffer B and the same dialysis buffer was used for protein dilutions. 19-point titrations were carried out using 200μM Mth R3035 in the syringe and 20μM FecB in the cell, whereas 13-point titrations were carried out using 300μM Rv3035 and 30μM FecB-His mutant protein, or 200μM Rv3035-His and 20μM FecB-His. Notably, the His-tag on FecB did not appreciably change the affinity of FecB for Rv3035. Curve fitting was carried out using the Malvern instrument analysis software.

Structure determination of Mth Rv3035 and the FecB-Rv3035 complex

Initial screening of Mth Rv3035 (15mg/mL) and FecB-Rv3035 complex (38mg/mL) were carried out in 96-well trays using a Mosquito liquid handler (SPT Labtech, Cambridge, MA) and commercially available crystallization screens by the hanging drop vapor diffusion method.

Mth Rv3035 alone

Diffraction-quality Mth Rv3035 crystals were grown with a crystallization reservoir of 0.1M sodium chloride; 0.1M HEPES, pH 7.5; 1.6M ammonium sulfate with Rv3035 at 15 mg/mL and a reservoir to protein ratio of 1:1 at room temperature. The crystals were cryocooled in mother liquor supplemented with 25% glycerol. Data was collected at SSRL 12-2 at the wavelength 1 Å. Data was processed in xds[54] to a resolution of 1.9 Å (table S1). A model of Mth Rv3035 was generated on the AlphaFold server[25] and was used for molecular replacement (MR) in phaser[55] in phenix. The MR solution placed two subunits in the asymmetric unit (ASU) and was improved by autobuild in phenix[56], and refined in phenix.refine[57]. Following autobuild, the N-terminal residues 10-37 were built *de novo* in coot[58]. The N-terminal 9 residues of Rv3035 could not be modeled for both subunits, and for subunit B, the last C-terminal residue also could not be modeled due to unresolved electron density. The model was further refined in phenix.refine and coot to a final R_{work}/R_{free} of 16.1 / 20.25 (table S1).

FecB-Rv3035 complex

831 Diffraction-quality crystals of the FecB-Rv3035 complex were obtained with a crystallization
832 reservoir of 3M sodium chloride; 0.1M Bis-Tris, pH 7.0 with a reservoir to protein complex ratio of
833 1: 1. To further improve diffraction quality of the FecB-Rv3035 complex, an additive screen was
834 performed (Hampton Research, Aliso Viejo, CA), with the final conditions used being a
835 crystallization reservoir of 3M sodium chloride; 0.1M Bis-Tris, pH 7.0; 3% trehalose, with the
836 Rv3035-FecB complex at 38mg/ml and a reservoir to protein ratio of 1:1. Crystals were
837 cryoprotected in reservoir solution with 25% glycerol and flash frozen with liquid nitrogen. Data
838 was collected at SSRL 12-2 at the wavelength 1 Å.

839 Data was processed in XDS[54] to a resolution of 3.3 Å (table S1). The phases were solved by MR
840 in phaser[55] in phenix, placing a single subunit of the deposited FecB structure (PDB ID 7UQ0,[7])
841 in the ASU in complex with a single subunit of the Mth Rv3035 structure solved above. The MR
842 solution was improved in autobuild and refined as described above in phenix.refine[57] and coot[58]
843 to a final R_{work}/R_{free} of 25.2/26.3 (table S1).

844

845 **Knockout construction**

846 Δ*rv3035* and Δ*fecB*Δ*rv3035* mutants were generated using a suicide plasmid approach as
847 previously described[59] with a few modifications. Constructs containing 500bp fragments
848 corresponding to regions upstream and downstream of *rv3035* were ordered from GenScript and
849 cloned into a temperature-sensitive deletion vector pDE43-XSTS to flank the zeocin resistance
850 cassette and generate pKO-XSTS-Zeo-*rv3035* via Gateway Cloning. Mtb WT and Δ*fecB* were
851 transformed with both the pKO-XSTS-Zeo-*rv3035* and a *rv3035* complementation plasmid
852 (pGMCS-T02-P*hsp60*-SD1-*rv3035*_A-HA) to generate a merodiploid strain since initial attempts
853 of generating the knockout with pKO-XSTS-Zeo-*rv3035* alone had failed. Transformants were
854 plated on Middlebrook 7H10 agar (BD #262710) containing 0.5% glycerol, 10% OADC (BD
855 #212351) and 25µg/mL Zeo (for WT) or 50µg/mL Hyg and 25µg/mL Zeo (for Δ*fecB*) and incubated
856 at 37°C until colonies were approx. 1mm in diameter. Colonies were tested for reporter gene XylE
857 activity directly on plates by addition of a drop of catechol solution (1g in 20mL water). After 30
858 minutes, candidate colonies that turned yellow were selected and grown in regular 7H9 with
859 appropriate antibiotics until they reached an OD_{580nm} of 1-1.5. Candidates were then grown on
860 7H10 agar with 10% sucrose at 37°C until colonies were approx. 1mm in diameter. Colonies were
861 test for reporter gene activity as above, but this time white colonies (that had successfully lost the
862 suicide plasmid) were selected. Genomic DNA (gDNA) was extracted from a few mutant
863 candidates and allelic exchange was confirmed by PCR using primers listed in table S6. To obtain
864 the final knockout mutants, we replaced the *rv3035* complementation plasmid integrated into attL5
865 with an empty plasmid containing an apramycin resistance cassette (pGMCA-OXOX).
866 Transformants were plated on 7H10 containing Zeo (or Zeo and Hyg) and 60µg/mL apramycin.
867 Δ*rv3035* and Δ*fecB*Δ*rv3035* mutants took about 6-8 weeks to form visible colonies. Candidate
868 mutants were selected and tested for streptomycin sensitivity in liquid culture as an indication that
869 the copy of *rv3035* (carrying streptomycin resistance) was successfully replaced in attL5. Finally,
870 gDNA was extracted for whole genome sequencing to confirm deletion of *rv3035* and insertion of
871 zeocin and apramycin cassettes.

872

873 **Cell envelope permeability assays**

874 BODIPY Fluorescent (FL) vancomycin (Invitrogen #V34850) uptake was performed as previously
875 reported[5] with a few modifications. Briefly, mid-log phase Mtb cultures were washed once and
876 adjusted to an OD_{580nm} of 2 in PBS and incubated with 2µg/mL of BODIPY FL vancomycin. 350µL
877 sample aliquots were taken at the 30 minutes incubation time point, washed twice in PBS 0.05%
878 Tween80, and resuspended in 350µL PBS. Negative control samples were treated the same way
879 but did not receive BODIPY FL vancomycin. 100µL of each sample was distributed in triplicate
880 wells in a black-sided 96-well plate. Fluorescence was measured (excitation wavelength of 485nm
881 and emission wavelength of 538nm) and normalized to the OD_{580nm} of the final suspension to
882 account for cell loss during washing steps.

883 For the calcein-AM (Invitrogen #C3099) uptake assay, mid-log phase cultures were adjusted to
884 an OD_{580nm} of 0.8 in regular 7H9 and 100µL aliquots were added to the wells of a black-sided 96-
885 well plate in triplicates. 100µL of calcein-AM (1µg/mL in 7H9 0.4% glucose) was added to the
886 wells resulting in a final concentration of 0.5µg/mL calcein-AM. Fluorescence was measured
887 (excitation wavelength of 495nm and emission wavelength of 520nm) at 2 minutes intervals over
888 a course of 60 minutes. Fluorescence was normalized to OD_{580nm} measured at 60 minutes.

889

890 **Spot assay**

891 Mig-log phase Mtb cultures were adjusted to an OD_{580nm} of 0.3 and 10-fold serial dilutions in PBS
892 0.05% Tween80 were spotted on 7H10 agar with 5µL per spot. Plates were incubated at 37°C
893 and imaged after 2-3 weeks. To confirm colony morphology alteration and growth defect of Δ*fecB*,
894 Δ*rv3035* and Δ*fecB* Δ*rv3035* mutants, plates were incubated for 4-5 additional weeks, after which
895 the phenotypes were unchanged.

896

897 **DMN-Tre labeling and flow cytometry**

898 Mid-log phase Mtb cultures were adjusted to OD_{580nm} of 0.5 in regular 7H9. For CRISPRi strains,
899 cultures were split into two flasks and 200ng/mL of ATc was added to one of the flasks 2-3 days
900 prior to labeling with DMN-Tre to pre-deplete the gene of interest. DMN-Tre probe[30] was added to
901 500µL of culture at a final concentration of 100µM. Samples were incubated at 37°C overnight for
902 approximately 20h. On the next day, cultures were spun down at 10,000rpm for 3 minutes, and
903 the supernatant containing DMN-Tre was discarded. Samples were fixed with 4% PFA (Biolegend
904 #420801) for 4h at room temperature. After two washes in PBS 0.05% Tween80, bacteria were
905 resuspended in PBS. Data collection was performed on a FACSymphony A5 Cell Analyzer (BD
906 Biosciences) at the Weill Cornell Medicine Flow Cytometry Core Facility using the 405nm violet
907 laser and the 405 [425/50] detector. Fluorescence data were obtained for 200,000 events per
908 sample and analyzed in FlowJo software (BD) by first gating on the bacterial population in the
909 side scatter versus forward scatter plot followed by calculation of the mean fluorescence intensity.

910

911 **Mouse infection**

912 Sixty-four female, eight-week-old *Mus musculus* C57BL/6 (Jackson Laboratories) were infected
913 with ~100 colony forming units (CFU)/mouse using an Inhalation Exposure System (Glas-Col).
914 Mice in the doxycycline group started to receive doxycycline chow 2 days before aerosol infection.
915 The FecB-TetON strain was grown to mid-log phase in the presence of 1µg/mL ATc, a single cell
916 suspension was prepared in PBS 0.05% Tween80 and then resuspended in PBS for a final
917 OD_{580nm} of 0.2. Lungs and spleen were homogenized in PBS and plated on 7H10 agar containing
918 1µg/mL ATc to determine CFU/organ at the indicated time points. This experiment was performed
919 in accordance with the Guide for the Care and Use of Laboratory Animals of the National Institutes
920 of Health, with approval from the Institutional Animal Care and Use Committee of Weill Cornell
921 Medicine.

922

923 **Quantification and statistical analysis**

924 Data analysis and generation of graphs were performed in Prism version 10.5 (GraphPad).

925

926 **Acknowledgements**

927 We thank Sae Woong Park (Weill Cornell Medicine) for sharing the Δ*mbtK* and Δ*mbtI* strains,
928 Carolina Trujillo (Weill Cornell Medicine) for assistance with the animal experiment, and Allison
929 Fay (Memorial Sloan Kettering Cancer Center) for her advice on the thin layer chromatography
930 experiment. We thank the staff of the University of Massachusetts Chan Medical School Mass
931 Spectrometry Facility and Kadamba Papavinasasundaram for their help with the pull-down
932 tandem mass spectrometry experiments. We thank the Kamariza Lab at the University of
933 California, Los Angeles for gifting an aliquot of the DMN-Tre probe. We thank the staff of the Weill
934 Cornell Medicine Genomics Resources Core Facility and Flow Cytometry Core Facility for their
935 contribution and advice on the RNA-seq and flow cytometry experiments, respectively. We thank
936 the staff of the Advanced Light Source at Berkeley National Laboratories and the Stanford
937 Synchrotron Radiation Lightsource for their invaluable help in data collection.

938 This material is based upon work supported by the National Science Foundation Graduate
939 Research Fellowship under Grant No. 2139291 and the Potts Memorial Foundation Pre-doctoral
940 Fellowship.

941

942 **References**

943 1. 2024 Global tuberculosis report.

944 2. Poulton, N. C. & Rock, J. M. Unraveling the mechanisms of intrinsic drug resistance in
945 Mycobacterium tuberculosis. *Front Cell Infect Microbiol* **12**, 997283 (2022).

946 3. Dulberger, C. L., Rubin, E. J. & Boutte, C. C. The mycobacterial cell envelope - a moving
947 target. *Nat Rev Microbiol* **18**, 47–59 (2020).

948 4. Jackson, M., Stevens, C. M., Zhang, L., Zgurskaya, H. I. & Niederweis, M. Transporters
949 Involved in the Biogenesis and Functionalization of the Mycobacterial Cell Envelope.
950 (2020) doi:10.1021/acs.chemrev.0c00869.

951 5. Xu, W. *et al.* Chemical Genetic Interaction Profiling Reveals Determinants of Intrinsic
952 Antibiotic Resistance in Mycobacterium tuberculosis. (2017) doi:10.1128/AAC.01334-17.

953 6. Staudenmaier, H., Van Hove, B., Yaraghi, Z. & Braun, V. Nucleotide sequences of the
954 fecBCDE genes and locations of the proteins suggest a periplasmic-binding-protein-
955 dependent transport mechanism for iron(III) dicitrate in Escherichia coli. *J Bacteriol* **171**,
956 2626–2633 (1989).

957 7. de Miranda, R. *et al.* Differentiating the roles of Mycobacterium tuberculosis substrate
958 binding proteins, FecB and FecB2, in iron uptake. *PLoS Pathog* **19**, (2023).

959 8. Wang, L. *et al.* Multiple genetic paths including massive gene amplification allow
960 Mycobacterium tuberculosis to overcome loss of ESX-3 secretion system substrates.
961 *Proc Natl Acad Sci U S A* **119**, e2112608119 (2022).

962 9. Leisching, G., Pietersen, R. D., Wiid, I. & Baker, B. Virulence, biochemistry, morphology
963 and host-interacting properties of detergent-free cultured mycobacteria: An update.
964 *Tuberculosis* **100**, 53–60 (2016).

965 10. Alland, D., Steyn, A. J., Weisbrod, T., Aldrich, K. & Jacobs, W. R. Characterization of the
966 Mycobacterium tuberculosis iniBAC promoter, a promoter that responds to cell wall
967 biosynthesis inhibition. *J Bacteriol* **182**, 1802–1811 (2000).

968 11. Schapira, M., Tyers, M., Torrent, M. & Arrowsmith, C. H. WD40 repeat domain proteins: a
969 novel target class? *Nature Reviews Drug Discovery 2017 16:11* **16**, 773–786 (2017).

970 12. Jinich, A. *et al.* Genome-wide co-essentiality analysis in Mycobacterium tuberculosis
971 reveals an itaconate defense enzyme module. *bioRxiv* 2022.09.27.509804 (2022)
972 doi:10.1101/2022.09.27.509804.

973 13. Li, S. *et al.* CRISPRi chemical genetics and comparative genomics identify genes
974 mediating drug potency in Mycobacterium tuberculosis. *Nature Microbiology 2022 7:6* **7**,
975 766–779 (2022).

976 14. Teufel, F. *et al.* SignalP 6.0 predicts all five types of signal peptides using protein
977 language models. *Nature Biotechnology 2022 40:7* **40**, 1023–1025 (2022).

978 15. Smithers, L., Olatunji, S. & Caffrey, M. Bacterial Lipoprotein Posttranslational
979 Modifications. New Insights and Opportunities for Antibiotic and Vaccine Development.
980 *Front Microbiol* **12**, 788445 (2021).

16. Drage, M. G. *et al.* Mycobacterium tuberculosis lipoprotein LprG (Rv1411c) binds triacylated glycolipid agonists of Toll-like receptor 2. *Nat Struct Mol Biol* **17**, 1088–1095 (2010).

17. Holm, L. & Rosenström, P. Dali server: conservation mapping in 3D. *Nucleic Acids Res* **38**, W545–W549 (2010).

18. Dejesus, M. A. *et al.* Comprehensive essentiality analysis of the Mycobacterium tuberculosis genome via saturating transposon mutagenesis. *mBio* **8**, (2017).

19. Bosch, B. *et al.* Genome-wide gene expression tuning reveals diverse vulnerabilities of M. tuberculosis. *Cell* **184**, 4579-4592.e24 (2021).

20. Seidel, M. *et al.* Identification of a Novel Arabinofuranosyltransferase AftB Involved in a Terminal Step of Cell Wall Arabinan Biosynthesis in Corynebacterianeae, such as Corynebacterium glutamicum and Mycobacterium tuberculosis. *Journal of Biological Chemistry* **282**, 14729–14740 (2007).

21. Liu, Y. *et al.* Structural insights into terminal arabinosylation of mycobacterial cell wall arabinan. *Nature Communications 2025 16:1* **16**, 1–16 (2025).

22. Poulton, N. C. & Rock, J. M. Unraveling the mechanisms of intrinsic drug resistance in Mycobacterium tuberculosis. *Front Cell Infect Microbiol* **12**, 997283 (2022).

23. Gupta, K. R. *et al.* An essential periplasmic protein coordinates lipid trafficking and is required for asymmetric polar growth in mycobacteria. *Elife* **11**, (2022).

24. Daffé, M. The mycobacterial antigens 85 complex – from structure to function and beyond. *Trends Microbiol* **8**, 438–440 (2000).

25. Abramson, J. *et al.* Accurate structure prediction of biomolecular interactions with AlphaFold 3. *Nature* **630**, 493–500 (2024).

26. Degiacomi, G. *et al.* Essentiality of mmpL3 and impact of its silencing on Mycobacterium tuberculosis gene expression. *Sci Rep* **7**, 1–8 (2017).

27. Fay, A. *et al.* Two accessory proteins govern MmpL3 mycolic acid transport in mycobacteria. *mBio* **10**, (2019).

28. Varela, C. *et al.* MmpL Genes Are Associated with Mycolic Acid Metabolism in Mycobacteria and Corynebacteria. *Chem Biol* **19**, 498–506 (2012).

29. Bansal-Mutalik, R. & Nikaido, H. Quantitative lipid composition of cell envelopes of Corynebacterium glutamicum elucidated through reverse micelle extraction. *Proc Natl Acad Sci U S A* **108**, 15360–15365 (2011).

30. Kamariza, M. *et al.* Rapid detection of Mycobacterium tuberculosis in sputum with a solvatochromic trehalose probe. *Sci Transl Med* **10**, (2018).

31. Birch, H. L. *et al.* Biosynthesis of mycobacterial arabinogalactan: identification of a novel α(1→3) arabinofuranosyltransferase. *Mol Microbiol* **69**, 1191 (2008).

1017 32. Gandotra, S., Schnappinger, D., Monteleone, M., Hillen, W. & Ehrt, S. In vivo gene
1018 silencing identifies the Mycobacterium tuberculosis proteasome as essential for the
1019 bacteria to persist in mice. *Nat Med* **13**, 1515–1520 (2007).

1020 33. Abrahams, K. A. & Besra, G. S. Mycobacterial cell wall biosynthesis: a multifaceted
1021 antibiotic target. *Parasitology* **145**, 116–133 (2018).

1022 34. Lissner, R. *et al.* A new role for lipoproteins LpqZ and FecB in orchestrating mycobacterial
1023 cell envelope biogenesis. *bioRxiv* 2025.06.19.660376 (2025)
1024 doi:10.1101/2025.06.19.660376.

1025 35. Jankute, M. *et al.* Disruption of mycobacterial aftB results in complete loss of terminal β(1
1026 → 2) arabinofuranose residues of Lipoarabinomannan. *ACS Chem Biol* **12**, 183–190
1027 (2017).

1028 36. Liu, Y. *et al.* Structural insights into terminal arabinosylation of mycobacterial cell wall
1029 arabinan. *Nature Communications 2025 16:1* **16**, 1–16 (2025).

1030 37. Patel, O. *et al.* Crystal structure of the putative cell-wall lipoglycan biosynthesis protein
1031 LmcA from Mycobacterium smegmatis. *Acta Crystallogr D Struct Biol* **78**, 494–508
1032 (2022).

1033 38. Taschner, M., Mourão, A., Awasthi, M., Basquin, J. & Lorentzen, E. Structural basis of
1034 outer dynein arm intraflagellar transport by the transport adaptor protein ODA16 and the
1035 intraflagellar transport protein IFT46. *Journal of Biological Chemistry* **292**, 7462–7473
1036 (2017).

1037 39. Kanao, T. *et al.* Reaction mechanism of tetrathionate hydrolysis based on the crystal
1038 structure of tetrathionate hydrolase from Acidithiobacillus ferrooxidans. *Protein Science*
1039 **30**, 328–338 (2021).

1040 40. Jahn, B. *et al.* Similar but Not the Same: First Kinetic and Structural Analyses of a
1041 Methanol Dehydrogenase Containing a Europium Ion in the Active Site. *ChemBioChem*
1042 **19**, 1147–1153 (2018).

1043 41. Yang, H. *et al.* Structure-Function Analysis of a Quinone-Dependent Dehydrogenase
1044 Capable of Deoxynivalenol Detoxification. *J Agric Food Chem* **70**, 6764–6774 (2022).

1045 42. Jackson, M. *et al.* Inactivation of the antigen 85C gene profoundly affects the mycolate
1046 content and alters the permeability of the Mycobacterium tuberculosis cell envelope. *Mol*
1047 *Microbiol* **31**, 1573–1587 (1999).

1048 43. Sparks, I. L. *et al.* Lipoarabinomannan mediates localized cell wall integrity during division
1049 in mycobacteria. *Nature Communications 2024 15:1* **15**, 1–17 (2024).

1050 44. Kilburn, J. O. & Takayama, K. Effects of ethambutol on accumulation and secretion of
1051 trehalose mycolates and free mycolic acid in Mycobacterium smegmatis. *Antimicrob*
1052 *Agents Chemother* **20**, 401–404 (1981).

1053 45. Culviner, P. H., Guegler, C. K. & Laub, M. T. A simple, cost-effective, and robust method
1054 for rrna depletion in rna-sequencing studies. *mBio* **11**, (2020).

1055 46. Liao, Y., Smyth, G. K. & Shi, W. The R package Rsubread is easier, faster, cheaper and
1056 better for alignment and quantification of RNA sequencing reads. *Nucleic Acids Res* **47**,
1057 (2019).

1058 47. Chen, S., Zhou, Y., Chen, Y. & Gu, J. Fastp: An ultra-fast all-in-one FASTQ preprocessor.
1059 *Bioinformatics* **34**, i884–i890 (2018).

1060 48. Liao, Y., Smyth, G. K. & Shi, W. featureCounts: an efficient general purpose program for
1061 assigning sequence reads to genomic features. *Bioinformatics* **30**, 923–930 (2014).

1062 49. Love, M. I., Huber, W. & Anders, S. Moderated estimation of fold change and dispersion
1063 for RNA-seq data with DESeq2. *Genome Biol* **15**, 1–21 (2014).

1064 50. Nandakumar, M., Prosser, G. A., De Carvalho, L. P. S. & Rhee, K. Metabolomics of
1065 mycobacterium tuberculosis. *Methods in Molecular Biology* **1285**, 105–115 (2015).

1066 51. Layre, E. *et al.* A Comparative Lipidomics Platform for Chemotaxonomic Analysis of
1067 Mycobacterium tuberculosis. *Chem Biol* **18**, 1537–1549 (2011).

1068 52. Wainberg, M. *et al.* A genome-wide atlas of co-essential modules assigns function to
1069 uncharacterized genes. *Nat Genet* **53**, 638–649 (2021).

1070 53. Lobstein, J. *et al.* SHuffle, a novel Escherichia coli protein expression strain capable of
1071 correctly folding disulfide bonded proteins in its cytoplasm. *Microb Cell Fact* **11**, 1–16
1072 (2012).

1073 54. Kabsch, W. XDS. *Acta Crystallogr D Biol Crystallogr* **66**, 125–132 (2010).

1074 55. McCoy, A. J. *et al.* Phaser crystallographic software. *J Appl Crystallogr* **40**, 658–674
1075 (2007).

1076 56. Terwilliger, T. C. *et al.* Iterative model building, structure refinement and density
1077 modification with the PHENIX AutoBuild wizard. *Acta Crystallogr D Biol Crystallogr* **64**,
1078 61–69 (2007).

1079 57. Afonine, P. V. *et al.* Towards automated crystallographic structure refinement with
1080 phenix.refine. *Acta Crystallogr D Biol Crystallogr* **68**, 352–367 (2012).

1081 58. Emsley, P. & Cowtan, K. Coot: Model-building tools for molecular graphics. *Acta*
1082 *Crystallogr D Biol Crystallogr* **60**, 2126–2132 (2004).

1083 59. Ganapathy, U. *et al.* Two enzymes with redundant fructose bisphosphatase activity
1084 sustain gluconeogenesis and virulence in Mycobacterium tuberculosis. *Nature*
1085 *Communications 2015 6:1* **6**, 1–12 (2015).

1086

1087

Main Figures

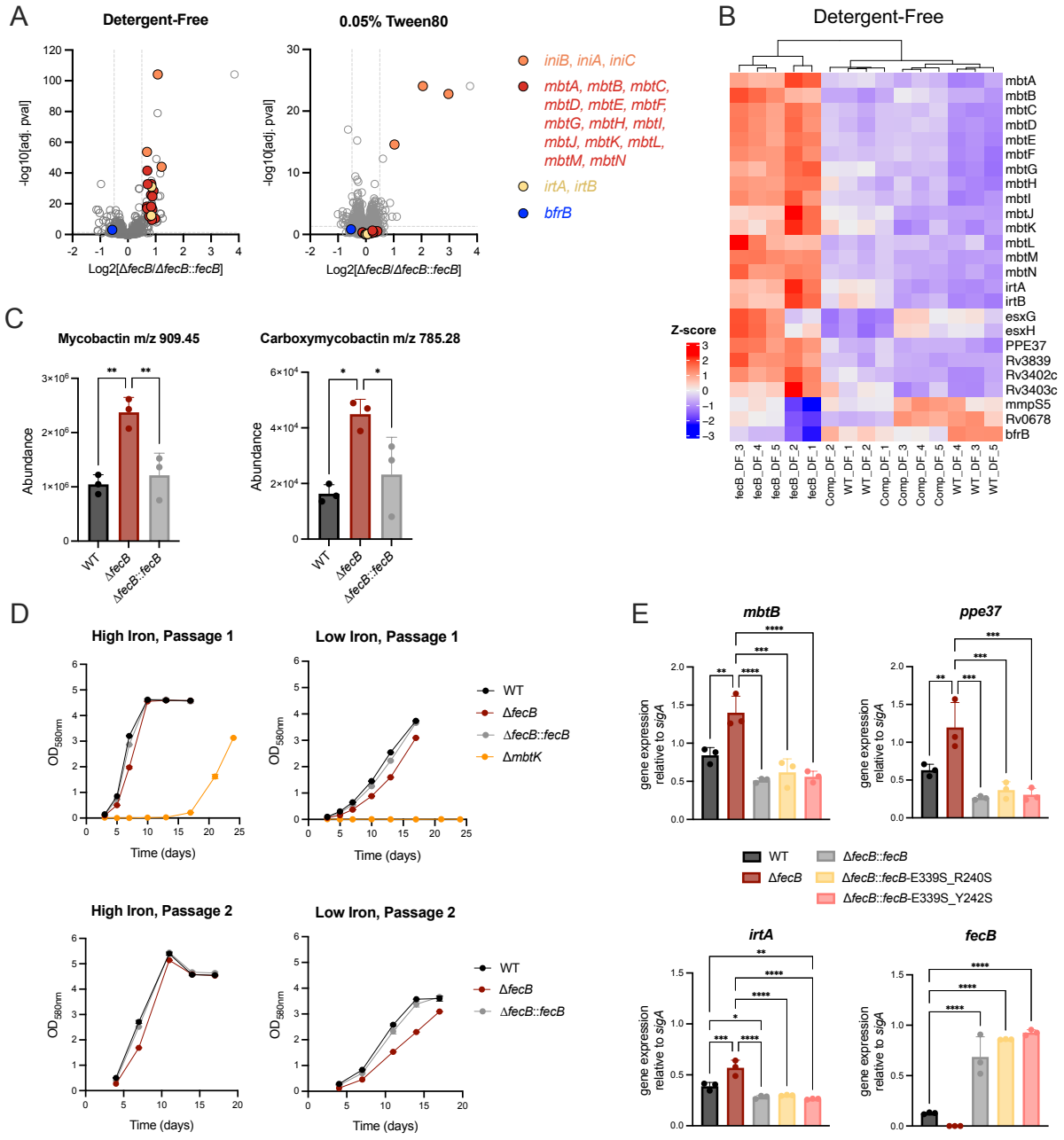

Figure 1. FecB plays a non-critical role in iron homeostasis in Mtb. (A) Volcano plots of transcriptome changes in Δ*fecB* compared to the complemented strain (Δ*fecB*::*fecB*) during log-phase growth in regular media without detergent or with 0.05% Tween80; highlighted genes are also differentially expressed in Δ*fecB* vs WT. (B) Heatmap of iron-related, differentially expressed genes (DEG) in strains grown in detergent-free media. DEGs were selected by padj ≤ 0.05 and |log2FC| ≥ 0.5; common hits in Δ*fecB* vs Δ*fecB*::*fecB* and Δ*fecB* vs WT are shown. (C) Relative abundance of representative mycobactin and carboxymycobactin species detected as [M+Fe-

2H]+ from lipid extracts analyzed by liquid chromatography-mass spectrometry (LC-MS). (D) Growth curves of iron pre-depleted strains in iron-chelated media with 160μM (high iron) or 1μM (low iron) ammonium ferric citrate (AFC). Cultures in low iron were grown until day 17 (Passage 1) and diluted to starting OD=0.025 in high/low iron media (Passage 2). Δ*mbtK* (mycobactin biosynthesis mutant) was used as a positive control that cannot grow in iron-limiting conditions. (E) Differential expression by reverse transcription quantitative PCR (RT qPCR) of representative iron-related genes (*mbtB*, *ppe37* and *irtA*) and *fecB* in strains grown in detergent-free media. Statistical significance in (C) and (E) was determined by one-way ANOVA and Tukey post-hoc test. Error bars: ±SD. N independent experiments = 2 with a total of five replicate cultures (A-B), 2 (C), 5 (D) and 1 (E) each performed with triplicate cultures.

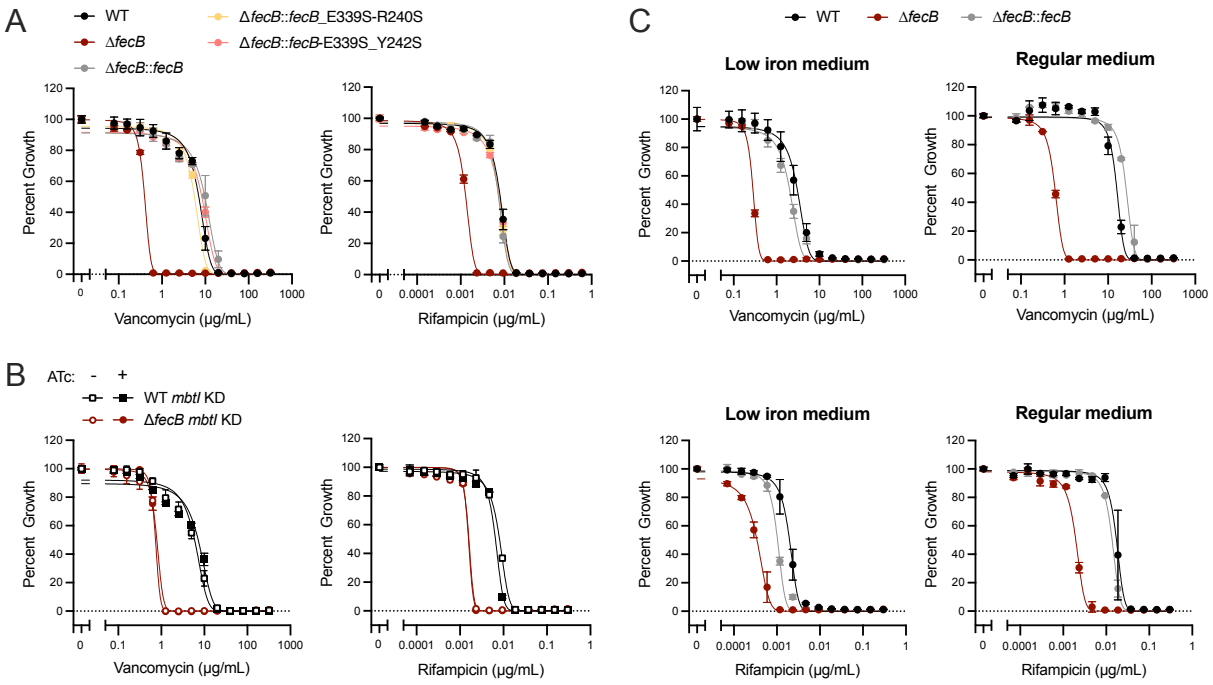

Figure 2. FecB's roles in iron homeostasis and multidrug resistance are not functionally related. MIC assays for vancomycin and rifampicin, percent growth calculated from no drug control wells. (A) Δ*fecB* complemented with FecB variants with lower binding affinity to ferric carboxymycobactin (Δ*fecB*::*fecB*-E339S_R240S and Δ*fecB*::*fecB*-E339S_Y242S) and control strains (day 14). (B) CRISPRi KD of *mbtI* in WT/Δ*fecB* in the absence or presence of ATc inducer (day 14). (C) WT, Δ*fecB* and Δ*fecB*::*fecB* strains in low iron (iron-chelated media with 1μM AFC) or regular media (day 21). Error bars: ±SD. N independent experiments = 2 (A, C), 1 (B), each performed with triplicate cultures.

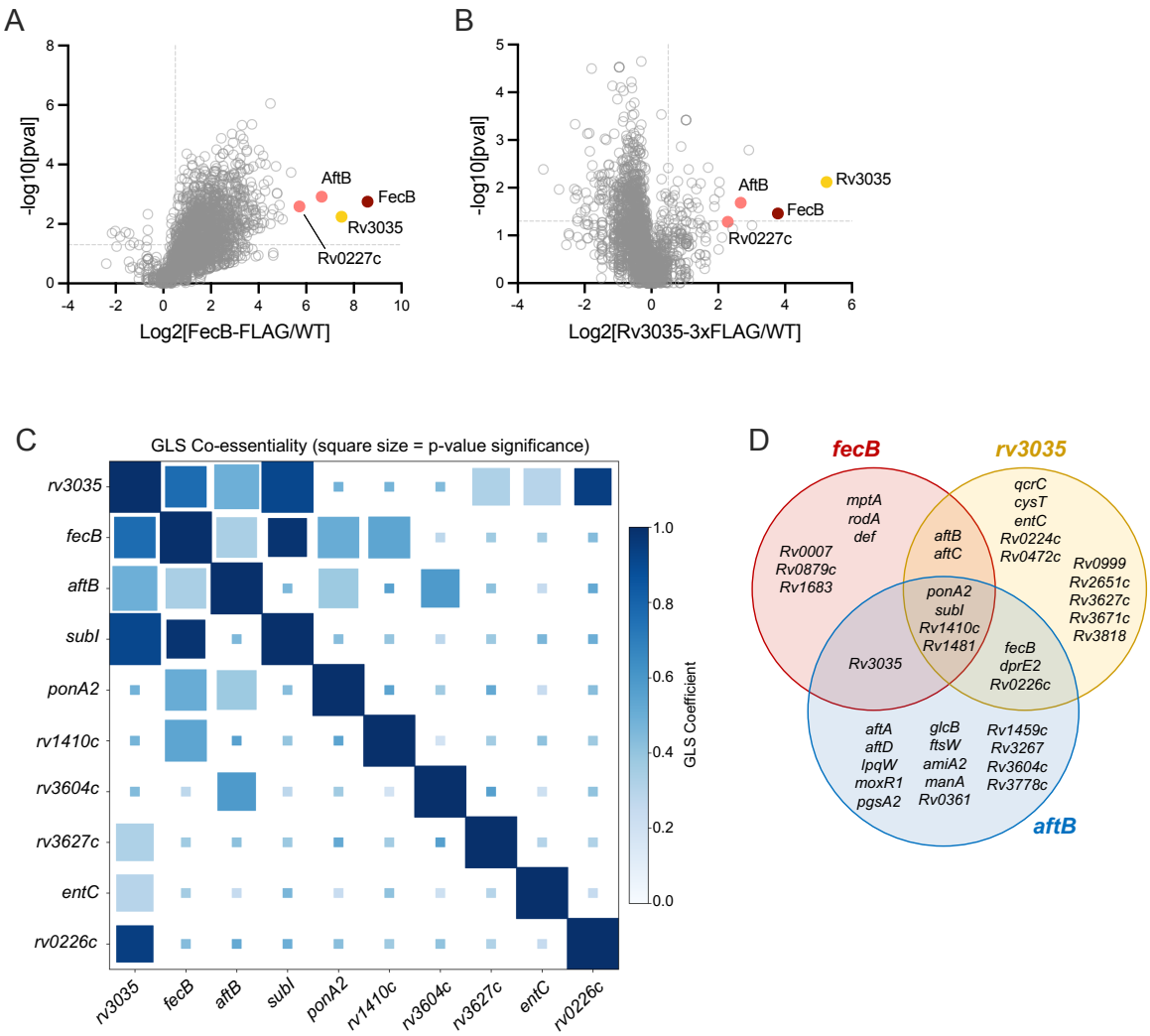

Figure 3. FecB and Rv3035 interact in Mtb and share essentiality profiles. Protein interaction profiling of (A) FecB and (B) Rv3035. FecB-FLAG and Rv3035-3xFLAG were immunoprecipitated from live Mtb and interacting proteins were identified by mass spectrometry. WT lysate was used a control for unspecific interactions. (C) Heatmap of co-essentiality Generalized Least Squares (GLS) coefficients for selected gene pairs. The genes shown were selected based on three "query genes": *fecB*, *rv3035*, and *aftB*. We included all gene pairs involving at least one of these queries that met a significance threshold of FDR-adjusted p-value < 0.001. Each square's color represents the GLS coefficient (i.e., the strength of co-essentiality), while size corresponds to statistical significance ($-\log_{10}$ of the FDR-adjusted p-value). Diagonal elements represent self-comparisons (each gene's $\log_2$ fold change profile against itself); while biologically uninformative, they are displayed at full size as a visual benchmark for perfect correlation. Some gene-gene combinations did not pass the significance threshold and are shown with smaller squares. (D) Venn diagram showing genes that are co-essential with *fecB* (red circle), *rv3035* (yellow circle) and *aftB* (blue circle), and their overlap. N independent experiments = 1 (A-B), each performed with triplicate cultures.

1135

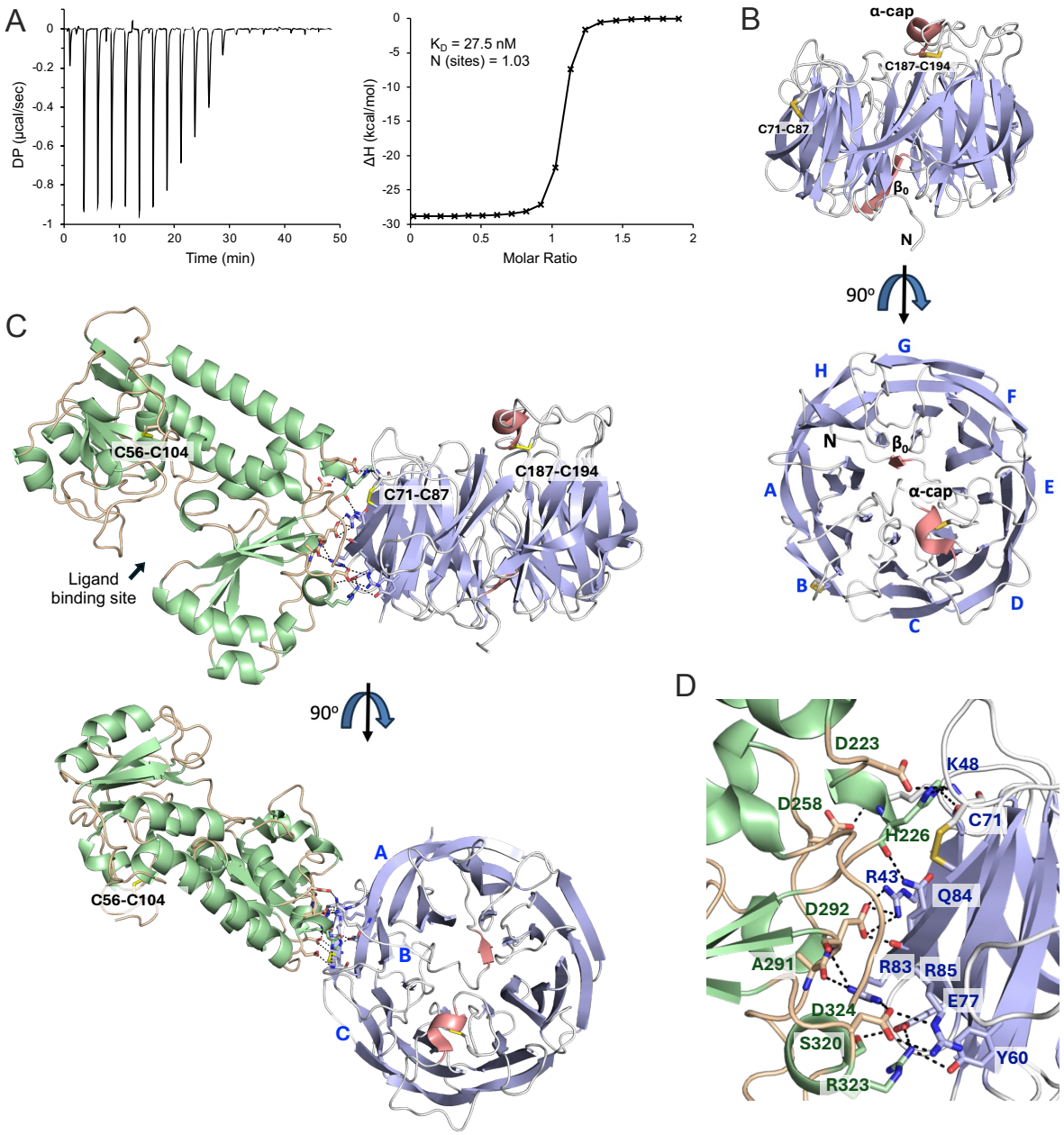

1136

1137 **Figure 4. Binding affinity of FecB and Rv3035 and X-ray crystal structures of Mth Rv3035**
1138 **and the FecB-Rv3035 complex.** (A) A 19-point ITC experiment was carried out by titrating 200µM
1139 Mth Rv3035 into 20µM Mtb FecB. The resulting thermogram is shown (left graph), resulting in the
1140 following calculated parameters: K_D = 27.5 ± 4.6 nM; N(sites) = 1.03 ± 0.004 (right graph). (B)
1141 Cartoon depiction of the structure of Mth Rv3035. The β-propeller fold is colored in light purple for
1142 β-strands and white for loops, each blade was assigned a letter, and the additional secondary
1143 structure elements are colored in pink. The disulfide bonds are shown in stick with yellow sulfur
1144 atoms. (C) Cartoon depiction of the structure of the FecB-Rv3035 complex. Rv3035 is colored as
1145 in (B). FecB secondary structure elements are colored in light green and loops in wheat. (D) A

zoom in of the interface of the FecB-Rv3035 complex with interacting residues shown in stick, and hydrogen bond and salt bridge interactions are represented in black dashed lines.

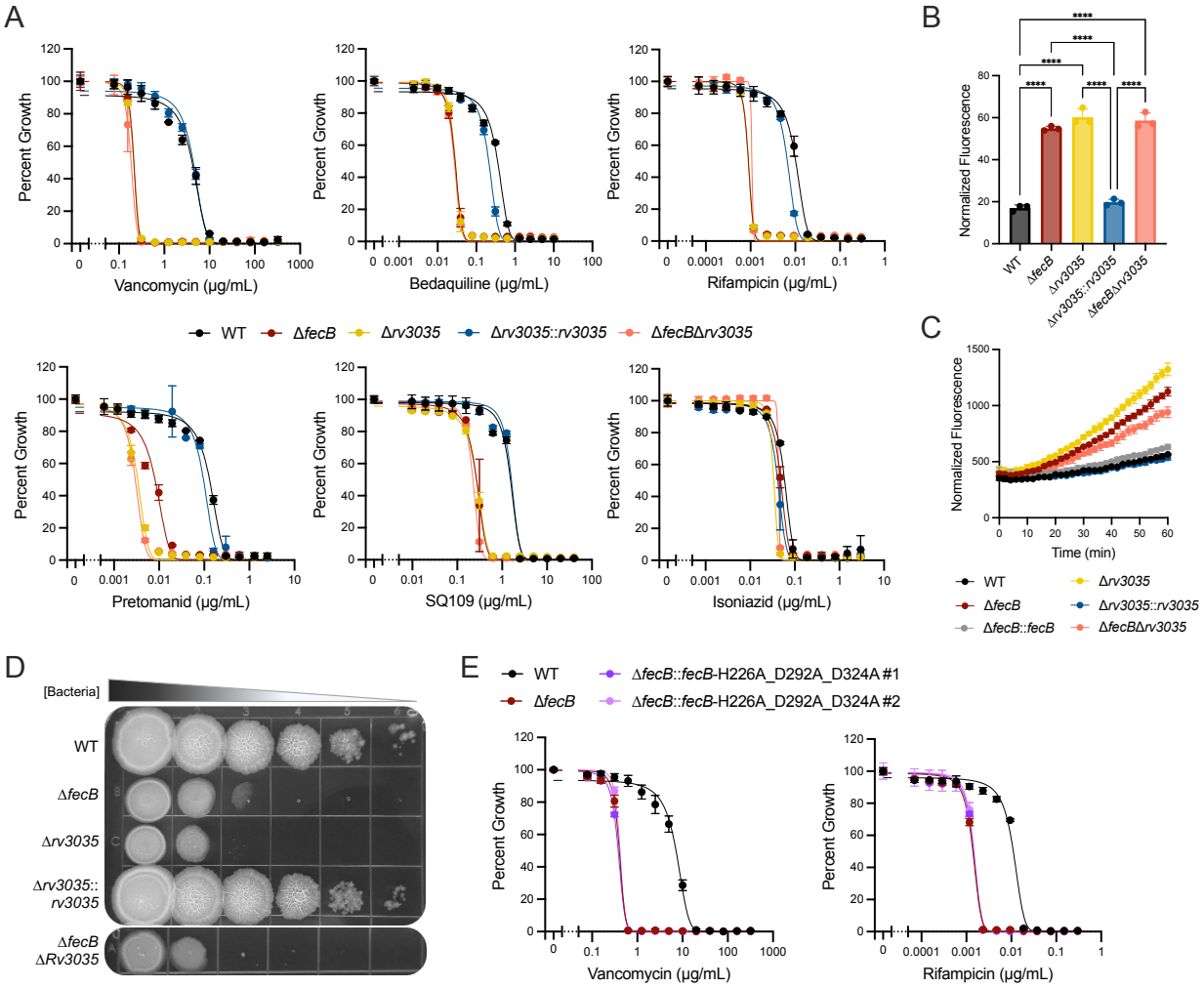

Figure 5. FecB and Rv3035 function in the same pathway that mediates cell envelope impermeability and antibiotic resistance in Mtb. (A) MIC assays for vancomycin, bedaquiline, rifampicin, pretomanid, SQ109 and isoniazid, percent growth calculated from no drug control wells (day 10). (B) BODIPY-vancomycin uptake after 30min of incubation, fluorescence intensity normalized by OD_{580nm}. Statistical significance was determined by one-way ANOVA and Tukey post-hoc test. (C) Calcein-AM uptake, fluorescence intensity normalized by OD_{580nm} at 60min. (D) Spot Assay. (E) MIC assay for vancomycin and rifampicin, percent growth calculated from no drug control wells. Δ*fecB* complemented with FecB triple mutant that does not bind Rv3035 (Δ*fecB*::*fecB*-H226A_D292A_D324A) and control strains (day 14), #1-2 indicate individual colonies (biological replicates). Error bars: ±SD. N independent experiments = 2 (A-D), 1 (E), each performed with triplicate cultures.

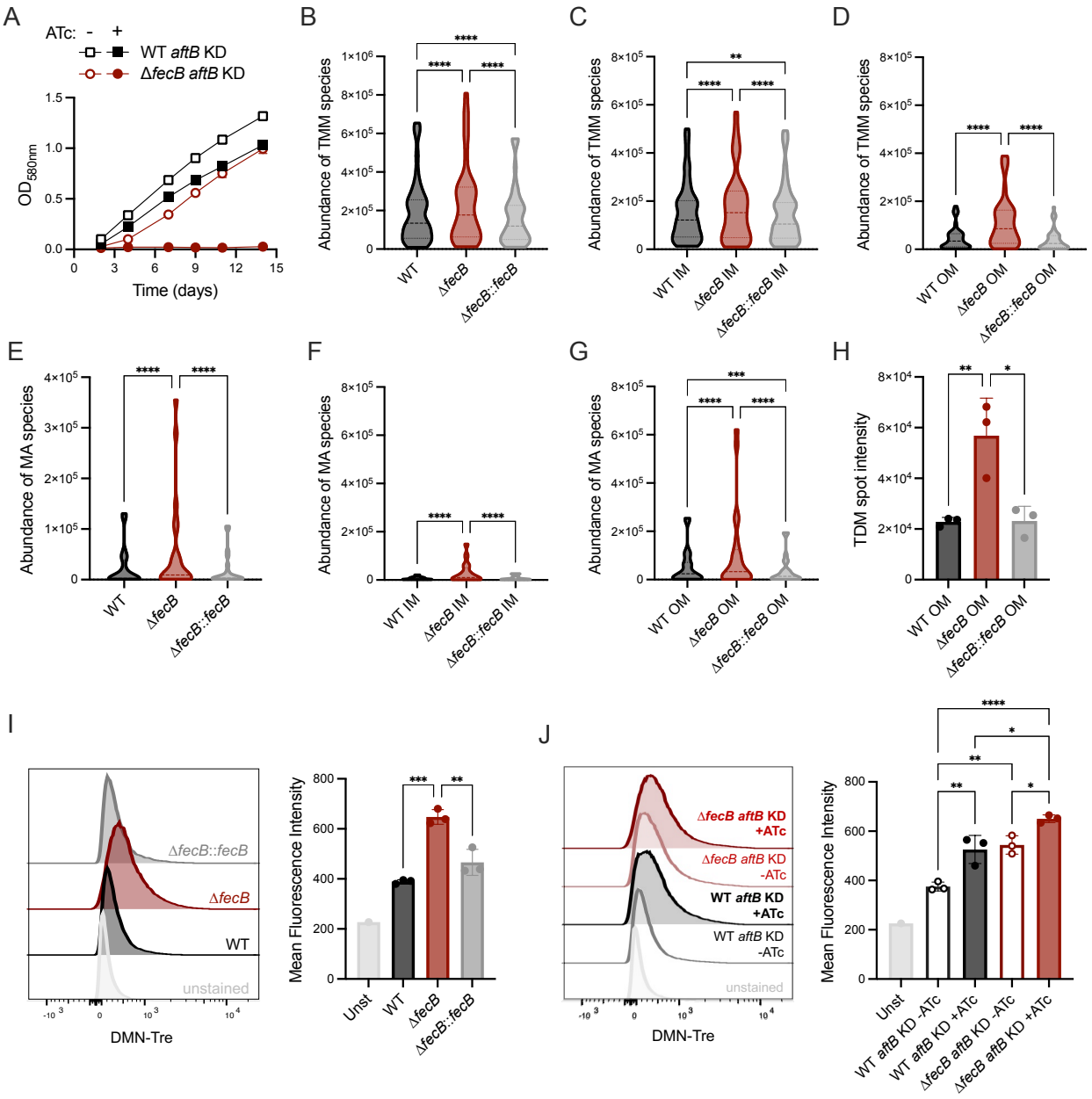

Figure 6. Enhanced vulnerability of *aftB* and accumulation of mycolates in Mtb Δ*fecB*. (A) Growth curve of CRISPRi KD of *aftB* in WT/Δ*fecB* in the absence or presence of ATc inducer; strains were grown in 384-well plate in standing conditions. Lipidomics analysis by LC-MS of total lipids (B, E) and fractions from AOT treatment (C-D, F-G) identifying (B-D) trehalose monomycolate (TMM) species and (E-G) free-mycolic acid (MA) species. (H) Trehalose dimycolate (TDM) spot intensity quantified from fig. S12E by densitometry analysis using ImageJ software. (I-J) Flow cytometry analysis of DMN-Tre labelled cells using 405nm laser and 525/50 channel. Representative histograms (left) and quantification (right) of mean fluorescence intensity of DMN-Tre probe. Unstained (Unst) WT was used as a control for autofluorescence. Statistical significance was determined by two-way (B-G) or one-way (H-J) ANOVA and Tukey post-hoc test.

1173 Error bars: ±SD. N independent experiments = 2 (A, I-J), 1 (B-H), each performed with triplicate
1174 cultures.

1175

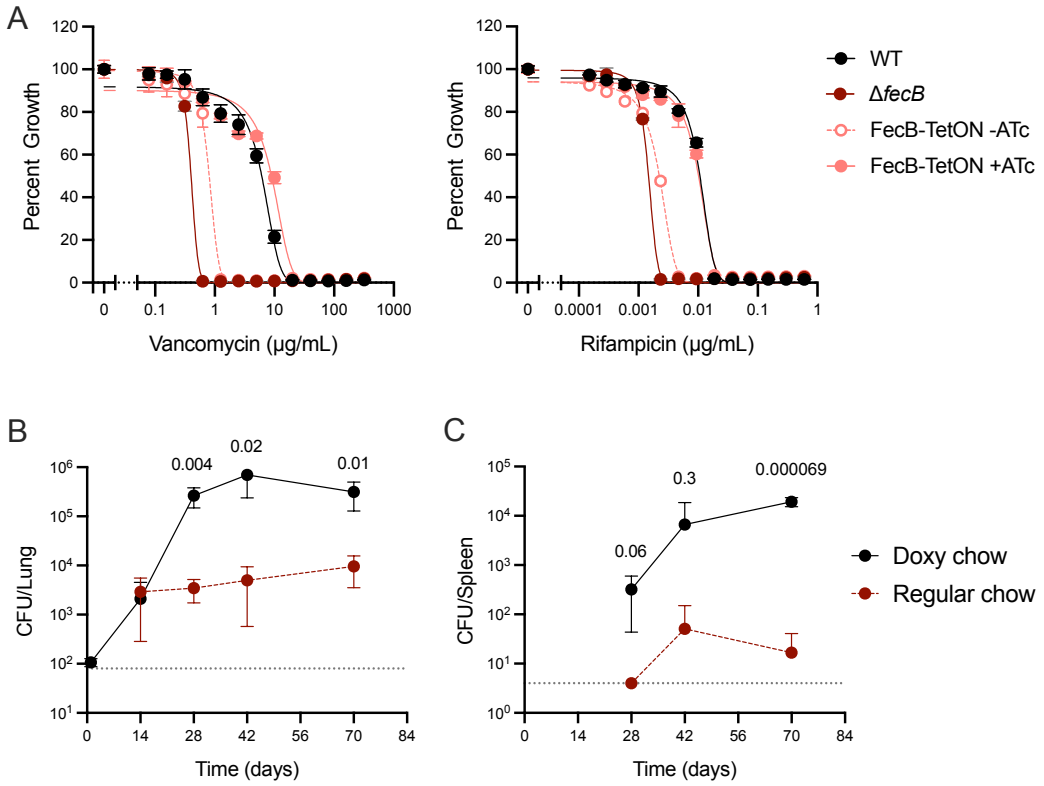

1176

1177 **Figure 7. FecB is required for Mtb virulence.** (A) MIC assays for vancomycin and rifampicin, in
1178 the absence or presence of ATc to induce *fecB* expression in the FecB-TetON strain (day 14).
1179 Percent growth calculated from no drug control wells. (B-C) Growth and persistence of FecB-
1180 TetON in the (B) lungs and (C) spleens of mice receiving doxy or regular chow. Data are average
1181 CFU counts from four mice per time point. Dashed black lines represent lower limit of detection.
1182 Statistical significance was determined by unpaired T-tests for each time point, p-value is shown
1183 above each pair analyzed. Error bars: ±SD. N independent experiments = 1 performed with
1184 triplicate cultures (A), 1 (B-C).

1185